MICROBIAL ADHESION TO MEDICAL IMPLANT MATERIALS:

AN ATOMIC FORCE MICROSCOPY STUDY

BY

RAY JENKINS EMERSON IV

A THESIS

SUBMITTED TO THE FACULTY OF

WORCESTER POLYTECHNIC INSTITUTE

IN PARTIAL FULFILLMENT OF THE REQUIREMENTS FOR THE

DEGREE OF MASTER OF SCIENCE

IN

CHEMICAL ENGINEERING

BY

----

6 JANUARY, 2004

APPROVED:

TERRI A. CAMESANO, PH.D., MAJOR ADVISOR
ASSISTANT PROFESSOR OF CHEMICAL ENGINEERING
WORCESTER POLYTECHNIC INSTITUTE

APPROVED:

RAVINDRA DATTA, PH.D., H.O.D
PROFESSOR OF CHEMICAL ENGINEERING
WORCESTER POLYTECHNIC INSTITUTE

Table of Contents

List of Tables

List of Figures

Acknowledgments

This, I think, is the hardest part to write in any paper requiring it.

First, I would like to give my sincere thanks to my advisor, Professor Terri A. Camesano, for her support, insight and guidance throughout this project. Without her, I would never have had the opportunity to complete this work.

Further, I would like to acknowledge Professor Robert W. Thompson for his thoughts, candor and aid in supporting my work. I hope I did a good job.

Next, I would like to thank the Department of Chemical Engineering, its faculty, staff and students for their assistance and patience as I pursued this Master's Degree. My sincere thanks also go to Worcester Polytechnic Institute for giving me the opportunity to stay on after my undergraduate career.

Thanks also go out to the National Science Foundation (Grants DGE-9355019 and BES-0238627), and the Petroleum Research Fund of the American Chemical Society (PRF Grant 38988-G2), for financial support of this work.

I would like to thank my co-workers in the lab, Nehal I. Abu-Lail and Bhupinder S. Arora, for their invaluable discussion, endless ideas, and infinite patience in the last two years. I hope the future holds countless amazing things for you.

Mr. Giacomo P. Ferraro and Mr. Douglas C. White are also sincerely thanked for their assistance and ingenuity in designing and maintaining my experimental equipment.

I would also like to recognize a few very special people who had a profound impact on me in my first six years at WPI. Thank you, Michael Bartley, Nichole Bisceglia, Michael Brady, Robert Bukofser, Caitlin Callaghan, Eugene Campbell, Robert Craig, Melissa Deschler, Pascal Eyriés, Sarah Haney, Carina Hart, Eric Kenney, Sally Nobrega, Paolo Paci, Fabien Ramat, Vincent Salemi, Brady Schulman, Justin Surpless, and Robert Tuttle for always being my friends, then and now. You helped me make this possible.

Finally, I would like to thank my family, friends and fraternity Brothers who supported me throughout this work. These are too many people to recognize, so I will simply say: Thank you all, from the bottom of my heart.

This manuscript is humbly dedicated to the memories of Mr. Ray J. Emerson, Jr., and Mrs. Kathryn F. White. Without them, my dream of a college education would have remained just that. I miss you both very much.

> PROGRESS, MAN'S DISTINCTIVE MARK ALONE,
> NOT GOD'S AND NOT THE BEASTS';
> GOD IS, THEY ARE.
> MAN PARTLY IS AND WHOLLY HOPES TO BE.
> - BROWNING, *A DEATH IN THE DESERT*

MICROBIAL ADHESION TO MEDICAL IMPLANT MATERIALS:

AN ATOMIC FORCE MICROSCOPY STUDY

1 – Abstract

Microbial infections of medical implants occur in more than 2 million surgical

cases each year in the United States alone. These increase patient morbidity and

mortality, as well as patient cost and recovery time. Many treatments are available, but

none are guaranteed to remove the infection. The purpose of this work is to examine the

initial events in microbial adhesion by simulating the approach and contact between a

planktonic cell, immobilized on an Atomic Force Microscope (AFM) cantilever, and a

biomaterial or biofilm substrate.

Distinct adhesive interactions exist between *Candida parapsilosis* and both

unmodified silicone rubber and *Pseudomonas aeruginosa* biofilms. Using *C.

parapsilosis* cells immobilized on AFM cantilevers with a silicone substrate, we have

measured attractive interactions with magnitude of 2.3 ± 0.5 nN (SD)[1] in the approach

portion of the force cycle. On *P. aeruginosa* biofilms, the magnitude of the attractive

force increases to 3.5 ± 0.75 nN (SD), and is preceded by a 2.5 nN repulsion at

approximately 175 nm from the cell surface. This repulsion may be attributed to steric

and electrostatic interactions between the two microbial polymer brushes.

Young's moduli for microbes and biofilms were calculated using Hertzian contact

models. These produced values of 0.21 ± 0.003 MPa (SD) for the *C. parapsilosis*-

silicone rubber system, and 0.84 ± 0.015 MPa (SD) for the *C. parapsilosis*-biofilm

---

[1] Values of error shown in this document reflect the standard deviation amongst repeated data sets. This is indicated by the symbol (SD).

system. This technique may be extended to calculate the work per unit contact area involved in the attractions in experimental data. For example, the work of adhesion using a spore probe is an order of magnitude greater for unmodified silicone rubber than for a *P. aeruginosa* biofilm. This indicates a high affinity for silicone rubber, and suggests that this material is vulnerable to infection by *C. parapsilosis in vivo*.

We have also demonstrated that AFM force curve analysis using established qualitative and quantitative models fails to accurately represent the physical interactions taking place between the probe and sample for the case where a polymer brush exists on the substrate, the probe, or both. As such, an approximate method defining the sample surface as the actual surface plus some vertical dimension associated with the maximum compressible thickness of the polymer brush is discussed.

Characterization of cell-biomaterial and cell-cell interactions allows for a quantitative evaluation of the materials used for medical implantation. It also provides a link between the physicochemical and physicomechanical properties of these materials and the nanoscale interactions leading to microbial colonization and infection. The goal of this research is to study this link and determine how best to exploit it to prevent microbial infections of medical implant materials.

2 – Literature Review

The various species of microbes, including bacteria, fungi and yeasts, are ubiquitous entities that both benefit and confound humankind's efforts to enrich their own lives. Adhesion of these microbes to different surfaces, including soil particles [20, 71], industrial bioreactors and heat exchangers [79, 106], foodstuffs [34, 69], medical implants [41, 46, 56] and human cells [24, 73], has spawned an entire field of research through which humanity seeks to exploit, and, in many cases, overcome the activities of creatures one one-millionth their size. The focus of the research presented in this manuscript will be on microbial adhesion to medical implants.

2.1 – Microbial Adhesion in Biomedical Systems

Every year, in the United States alone, over 20 million surgical procedures are performed [56]. Each procedure requires temporary and/or permanent implantation of a medical device. The materials chosen for implantation, predominantly hydrophobic polymers, are noted for their biocompatibility and biostability *in vivo* [48]. For all these benefits, however, the materials prove to be adequate sites for microbial adsorption and growth, often leading to infection. Ultimately, of those 20 million procedures, 10% result in implant infections; in specific devices, such as the total artificial heart (polyurethane), this value can reach 30% [41]. As a specific example, we may look at the central venous catheter, infections of which are recorded at a rate of 200,000 per year in the United States alone [46].From a financial point of view, these infections generate over $11 billion annually for additional patient treatment [87]. These values increase each year as the total number of medical procedures performed increases.

On implantation, a medical device is immediately coated with physiological molecules (fluids, peptides, etc.), forming a conditioning film [13, 82]. Regardless of the material's surface chemistry at implantation, a gradual buildup of these molecules changes the surface to one easily colonized by microbes. Microbes, either actively or passively transporting to the implant surface, can reversibly adsorb to the biomaterial. Over time, this sorption becomes irreversible, and is often followed by the secretion of extracellular polysaccharides (EPS), surface growth, and biofilm formation. It is after the formation of a biofilm, when the microbes in the film are least susceptible to the host's immune response and external antimicrobial treatments, that the cascade of biochemical events associated with an infection begins within the microbial cells. This may include the secretion of a variety of toxic substances, of additional protective EPS, or of quorum-sensing autoinducer molecules, which signal nearby cells to initiate similar activity [41].

2.1.1 – Available Treatments for Biomedical Implant Infections

The mechanics of adhesion in medical environments, leading to patient infection, were discussed above. Once infection sets in, a variety of treatments are available. Each, however, has disadvantages. Global treatment, either by oral or intravenous antibiotic, may kill many microbes, but is rate-limited in transporting the antibiotic through infection-associated biofilms [87]. Further, treating infection systemically may result in killing beneficial microbes, such as those that reside in the gut and aid digestion [92]. Local treatment is accomplished by coating or impregnating an implant with antimicrobial compounds. Due to transport limitations of the antimicrobial into the environment, however, this method may never induce a concentration lethal to cells, and

may in fact allow cells to become resistant to the antimicrobial [46]. Once the implant is coated with physiological molecules, this limitation becomes more significant.   One preventative treatment is the careful integration of tissue around the implant at the time of surgery, giving somatic cells an advantage in the so-called "race for the surface" [41]. However, the extent of tissue integration is evaluated by the surgical team and is highly subjective. Currently, the only sure way to eradicate an implant infection once it has established itself is to excise the implant and all surrounding infected tissue.   This increases patient cost and recovery time, as well as risk of subsequent infections due to additional surgeries.

2.1.2 – Biofilms

While bacteria are commonly thought to be free-swimming organisms, the majority of their life cycle is spent in a sessile state [25]. After initial adhesive events take place, the immotile microbes may begin to form a structure known as a biofilm. A biofilm is a poly-laminar, often polymicrobial, arrangement of microbial cells and exopolysaccharide (EPS) material which affords many metabolic and protective benefits for the cells [9, 110].   Once a biofilm has successfully formed, specific metabolic processes begin. These may include the degradation of substrata, acquisition of environmental pollutants, secretion of protective EPS matrix, and the secretion of toxins into the environment.

Biofilms were first identified by Anton van Leeuwenhoek, who examined oral gingival plaque under one of the first light microscopes in the late 1600's, and identified the "wee beasties" therein [30]. Three hundred years later, ZoBell and Anderson [115]

5

identified biofilms in marine environments. Since that time, biofilms have been identified as the predominant stage of microbial life, and have been shown to be extremely important in environmental, industrial and medical concerns [26, 27].

A simplified mechanistic view of biofilm formation is shown in Figure 1, which details the processes of initial adhesion, due to specific and non-specific physicochemical interactions, growth and diversification to include multiple microbial species [13].
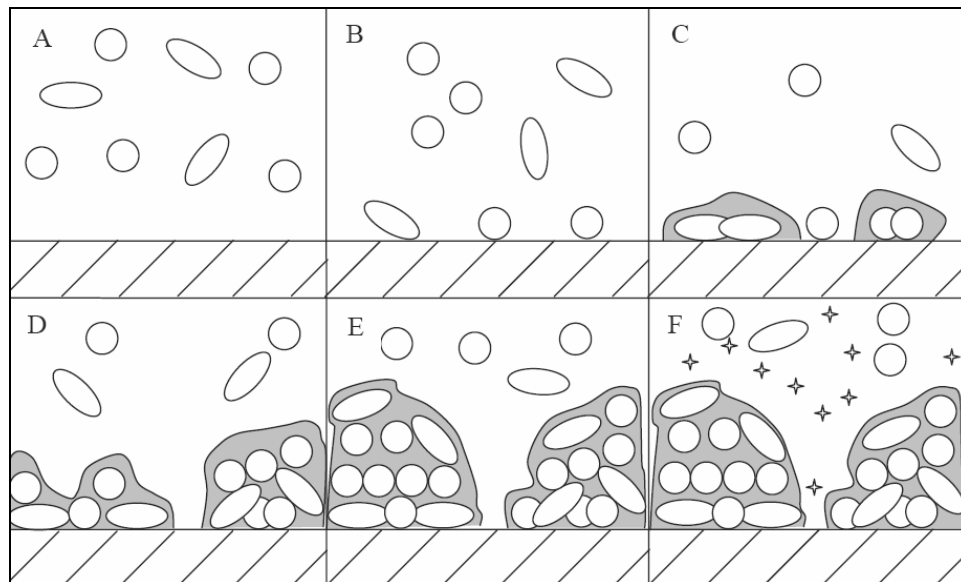
Figure 1 – Diagram describing the formation and growth of a microbial biofilm over time. Cells initially bind and secrete EPS. Other cells adhere, causing the biofilm to thicken. Once the film has grown to a sufficient maturity, virulence factors produced by the cells may be secreted into the bulk phase. Adapted from [13].

The biofilm is a homeostatic structure, meaning it is capable of self-regulation of physiological processes (e.g., metabolism, transport) in response to fluctuations in environmental conditions [110]. This is accomplished by the formation of channels, which act as a primitive circulatory system and allow for rudimentary transport of water and nutrients to the lower layers of the structure. Further, the biofilm provides significant protection against environmental factors (e.g., temperature, surrounding chemical composition). The inherent thickness of the film allows cells nearer the substratum to

6

survive and reestablish the colony, while cells nearer the external surface perish. This protection is of particular importance in pathogenic microbial strains, as it allows the microbes to secrete toxins into the host without vulnerability to host antigenic responses. In many cases, the biochemical processes leading to toxin production do not commence until a biofilm has formed, shielding the microbes from host antigenic responses. Any host immune activity or medical treatment seeking to eliminate the microbial infection will be less effective on a biofilm than on planktonic organisms as a result of this shielding. In clinical tests, microbes growing in biofilms were shown to be at least 500 times more resistant to antimicrobial therapies than their planktonic counterparts [27]. Where most existing antimicrobial chemicals have been developed using planktonic cells, which grow more rapidly and easily than biofilms, we are faced with the difficulty of having a tool available that is not able to fulfill its initial purpose.

Diversification of the film also aids in biofilm resistance to antimicrobial therapy, in that the chemical agents that effectively eliminate some microbes may not necessarily work on other species, or even on strains of the same species. Also, even if all microbes within the film are killed by medical or industrial treatment, the superstructure of the film may still remain, providing a suitable binding domain for other microbes, along with a high concentration of useable nutrients. Such a situation creates extreme difficulties for engineers and medical professionals seeking to remove biofilms once they have formed on surfaces.

2.1.3 – Relevant Microbes

A large number of different microbes may be responsible for infections of medical devices [41, 56, 87], a representative list of which may be seen in Table 1. These are classified according to chemical properties of the bacterial cell wall and gross cell morphology. "Gram-positive" and "Gram-negative" refer to a chemical assay, developed by Hans Christian Gram in 1844, used to characterize relative peptidoglycan and lipid content of the cell wall [114]. Gram-positive cells are able to retain the dye Crystal Violet, and have a higher content of peptidoglycan and lipid in the cell wall. Conversely, Gram-negative cells cannot retain this stain and have a lower relative peptidoglycan and lipid content. "Cocci" and "bacilli" are morphological terms referring to either ball-shaped (coccus) or rod-shaped (bacillus) cells. Fungi, being eukaryotic organisms while bacteria are prokaryotic, cannot be classified according to these terms, and are therefore presented separately.

Table 1 – List of clinically relevant microbes (Adapted from [46]).

Gram-Positive Cocci	Gram-Negative Bacilli	Fungi
Staphylococcus aureus	*Escherichia coli*	Candida spp.
Staphylococcus epidermidis	*Escherichia faecalis*	*Saccharomyces cerevisiae*
Staphylococcus marcescens	*Escherichia faecium*	
Staphylococcus maltophilia	*Pseudomonas aeruginosa*	
Coagulase-negative	Klebsiella spp.	
Staphylococci	Enterobacter spp.	
	Actinobacter spp.	

Each of the different strains shown above, as well as many other pathogenic species not referenced, are widely different in their affinities for different substrata, methods of infection, and susceptibility to antimicrobial therapies *in vivo* [46, 68]. This leads to difficulties in creating materials that microbes cannot adhere to, and in formulating medications that are effective in eradicating established infections. Since, in many cases, the microbes do not secrete toxic substances until they have formed a protective biofilm, these difficulties are significantly increased.

For this study, two model microbes were chosen based on their frequency of clinical isolation, pathogenicity, and ease of acquisition and handling.

2.1.3.1 – *Pseudomonas aeruginosa*

Pseudomonas aeruginosa is a Gram-negative bacterium that is omnipresent in both environmental and clinical settings [38, 65, 66]. While not a threat to healthy individuals, this microbe is categorized as an "opportunistic pathogen," an organism that can cause additional illness in patients who are previously immune-compromised. *P. aeruginosa* is isolated in almost 99% of all cases of bacteremia, most commonly from keratitis of the ocular cornea, and from infections associated with burn wounds. It is also found in secreted sputum from cystic fibrosis patients [65]. An image of a single *P. aeruginosa* cell may be seen in Figure 2.
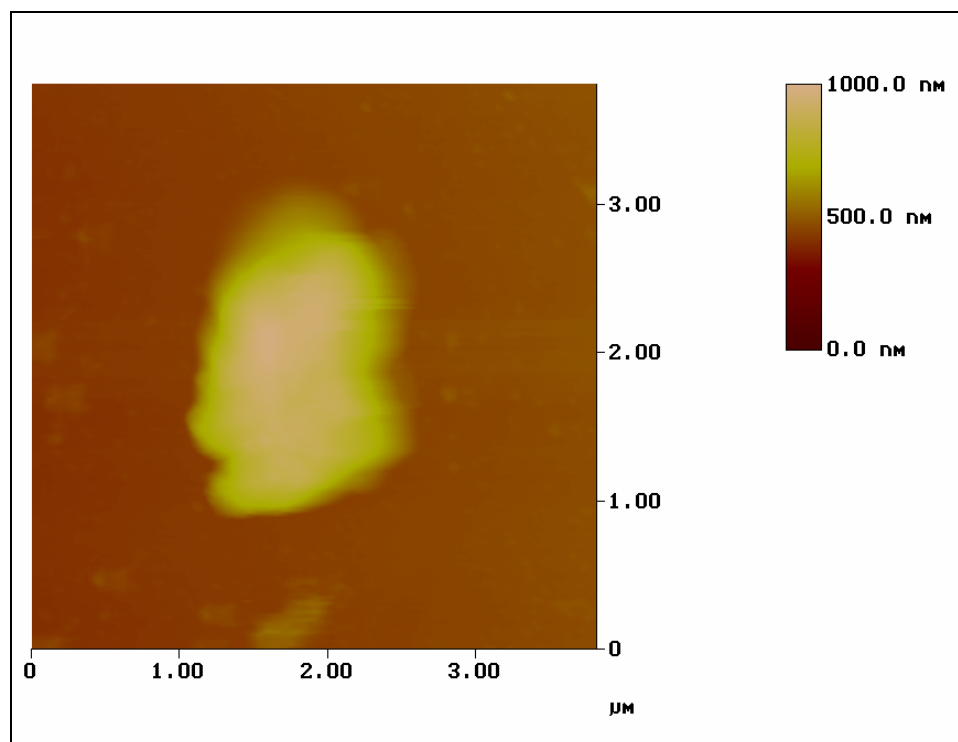
Figure 2 – TappingMode™ AFM image of *P. aeruginosa* ATCC 10145 under distilled, deionized water.

P. aeruginosa is one of the most-studied pathogens on record, owing to its ubiquity in the environment, as well as its versatility in adapting to a number of different surroundings [38, 85]. *P. aeruginosa* has been shown to possess one of the largest microbial genomes, and that the sequence of DNA is highly conserved (> 90%) from strain to strain [91, 111]. This conservation includes a number of different virulence factors and regulatory systems. Further, the genome contains large islands capable of integrating new genetic data through horizontal transfer. While horizontal gene transfer is common in many bacterial strains, *P. aeruginosa* shows a distinct talent for this difficult process, frequently obtaining information from its own and widely different microbial species.

P. aeruginosa's versatility and adaptability extend into its abilities to cause infection [65]. Virulence factors include pili, flagella, lipopolysaccharides, exotoxins, exoenzymes, and a number of other mechanisms by which this organism inflicts injury upon medical patients. These factors are all related to genes expressed solely during the sessile biofilm-phase. Understanding the adhesion mechanisms of this microbe at the scale these mechanisms occur would greatly benefit many thousands of medical patients each year.

2.1.3.2 – *Candida parapsilosis*

For many years, *Candida parapsilosis* has been a relatively minor isolate from nosocomial infections [72, 84]. Recent studies, however, have shown that this pathogen has become much more common, and is only exceeded in isolation frequency by *C. albicans* in hospital-acquired fungal infections. An image of *C. parapsilosis* may be seen in Figure 3.
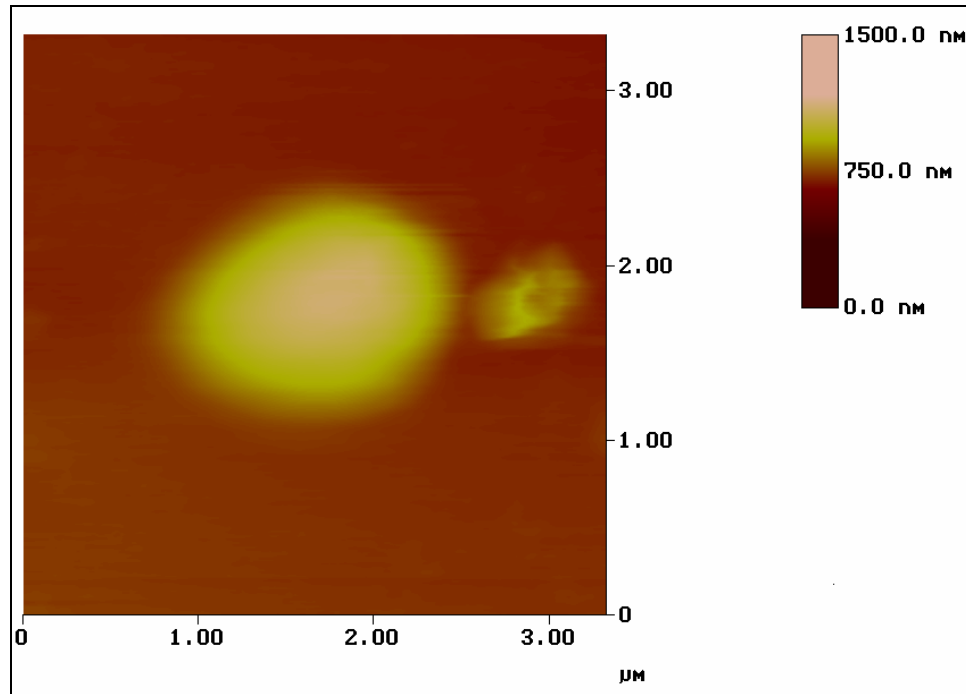
Figure 3 – TappingMode™ AFM image of *C. parapsilosis* ATCC 90018 under distilled, deionized water.

C. parapsilosis is also an opportunistic pathogen, and has a remarkable ability for horizontal transmission [64, 107]. This refers to the ease with which the cells may be transmitted from one individual to another. In the case of *C. parapsilosis*, horizontal transmission is a very common and very rapid mode of cellular dissemination from patient to patient. This microbe is commonly found in infections of medical implants, most especially those of implantable central venous catheters and bronchoscopes [59, 77].

The increasing isolation of *C. parapsilosis* among medical fungemiæ, its ease of transmission, and extreme virulence in medical infections dictate that this microbe must be understood. Information regarding its affinity for different biomaterial surfaces will increase the body of knowledge available for this organism, and will aid in finding methods to circumvent its adhesive and infective capabilities.

2.1.4 – Relevant Materials

Many of the devices implanted into medical patients contain polymeric materials. From a thermodynamic standpoint, most of these are hydrophobic in nature, since hydrophobic materials tend to be more biocompatible and biostable [48]. A list of several common biomaterials, and their uses, may be seen in Table 2. Each of these materials is susceptible to microbial infection. The exact probability that an implant will become infected, however, is dependent upon a number of factors, including the number and type(s) of microbes present, the exact chemical composition of the surrounding media (e.g., inside a blood vessel or the urinary tract), and the patient's overall health. As such, no quantitative data may be given at this point as to how likely, in a broad sense, each material is to be infected.

Table 2 – List of commonly-used medical device materials and their applications (Adapted from [38]). Abbreviations for each material are shown in parentheses.

Poly(dimethyl siloxane)	(PDMS)	
Pacemakers	Arteriovenous shunts	Intravascular devices
Cerebrospinal fluid shunts	Urological catheters	Peritoneal dialysis catheters
Mammary prostheses	Voice prostheses	
Polyethylene	(PET)	
Cerebrospinal fluid shunts	Intravascular devices	Orthopedic implants
Poly(ethylene terephthalate)	(PETE)	
Left ventricular assist devices	Prosthetic heart valves	Total artificial heart
Vascular grafts	Arteriovenous shunts	Intravascular devices
Peritoneal dialysis catheters	Mammary prostheses	
Poly(methyl methacrylate)	(PMMA)	
Bone cement	Cranioplastic implants	Intraocular artificial lens
Polypropylene	(PP)	
Abdominal wall prostheses	Intravascular devices	
Poly(tetrafluoro ethylene)	(PTFE)	
Vascular grafts	Arteriovenous shunts	Intravascular devices
Abdominal wall prostheses		
Polyurethane	(PU)	
Left ventricular assist device	Total artificial heart	Intravascular devices
Mammary prostheses	Pacemakers	

While excellent materials, in that they perform their designed task *in vivo*, and do not themselves cause additional harm to the patient, they are adequate sites to which microbes may bind, form biofilms, and release virulence factors [13]. This is predominantly due to similarities (*viz.* hydrophobicity) between molecules in the environment, the microbial colonizers and the biomaterial substrate. Biological molecules (e.g. proteins) physisorbed to the materials provide a conditioning film which makes the surface even more welcoming to microbes [87, 92].

As a solution to this problem, designers have introduced implant devices which are coated or impregnated with antimicrobial agents [46]. This provides a high implant-surface concentration of the antimicrobial, and a chemical gradient as the agent diffuses into the surroundings. Given the heterogeneity of the implantation environment (e.g., blood and other fluids contacting the devices, differences in patient chemistry), however, it is not likely that all patients will receive a sufficient systemic dose of the agent to kill all cells present. And, if this dose is achieved, it is very likely that beneficial microbes will be killed as well.

2.2 – Atomic Force Microscopy

The atomic force microscope (AFM) was invented in 1986 by Gerd Binnig, Calvin Quate (Stanford University) and Christoph Gerber (IBM) [2]. At that time, IBM's scanning tunneling microscope (STM) was the main tool for achieving atomic resolution of sample surfaces, but was limited to examination of conductive materials. The goal of the AFM was to provide the lateral resolution seen in the STM, while allowing for the examination of nonconductive surfaces in a nondestructive manner [10]. Further

development of the AFM has allowed for nanometer lateral resolution in topographical imaging of samples [18].

Since its inception, the AFM has been applied to a number of widely disparate fields. These include surface characterization of semiconductive and insulating materials [10], measurement of atomic bond rupture-forces between organosilane monolayers [109], and a variety of biological applications, including the study of the physicochemical properties of microbial surfaces [33], characterization of lectin-carbohydrate interactions at the nanoscale [95], measurement of the forces between complementary DNA strands [58], and characterization of bacterial-biomaterial interactions via functionalization of the AFM probe with biomaterial spheres or confluent microbial lawns [75, 80, 81].

2.2.1 – Basic Theory of Atomic Force Microscopy

The AFM is, most simply, a hybrid of IBM's STM and a stylus profilometer. The latter uses a sharp cantilever-mounted probe affixed with a mirror to magnify surface features onto photographic paper. A light source is shined into the mirror, which reflects onto the paper. As the cantilever scans across the surface, it deflects as it interacts with various surface features. Deflections are then translated to the photographic paper by changes in the intensity of the light from the mirror. Depending on the placement of the photographic paper in relation to the sample and the sharpness and compliance of the cantilever, the stylus profilometer is capable of resolutions up to 1000X [1, 10]. Combining this principle with the STM, however, allowed for resolutions at the atomic scale.

A generalized schematic of the AFM is shown in Figure 4. A solid-state laser diode generates a beam, which passes through the scanner head. The beam reflects from the back of the cantilever, into a split photodiode sensor. A sharp probe is affixed to the underside of the cantilever, which tracks height/interaction force differences in the sample surface, causing the cantilever to deflect and changing the incident angle of the laser on the photodiode. Data recorded by the photodiode is then translated into deflection voltage and separation distance, allowing the computer software to maintain a feedback loop of either constant cantilever deflection/interaction force (Contact mode) or constant cantilever oscillation amplitude (TappingMode™), which leads to intermittent contact between the probe and the sample. TappingMode™ affords several benefits over contact mode, in that intermittent contact allows for increased lateral resolution of soft and/or hydrated samples, and decreased damage to the sample surface.
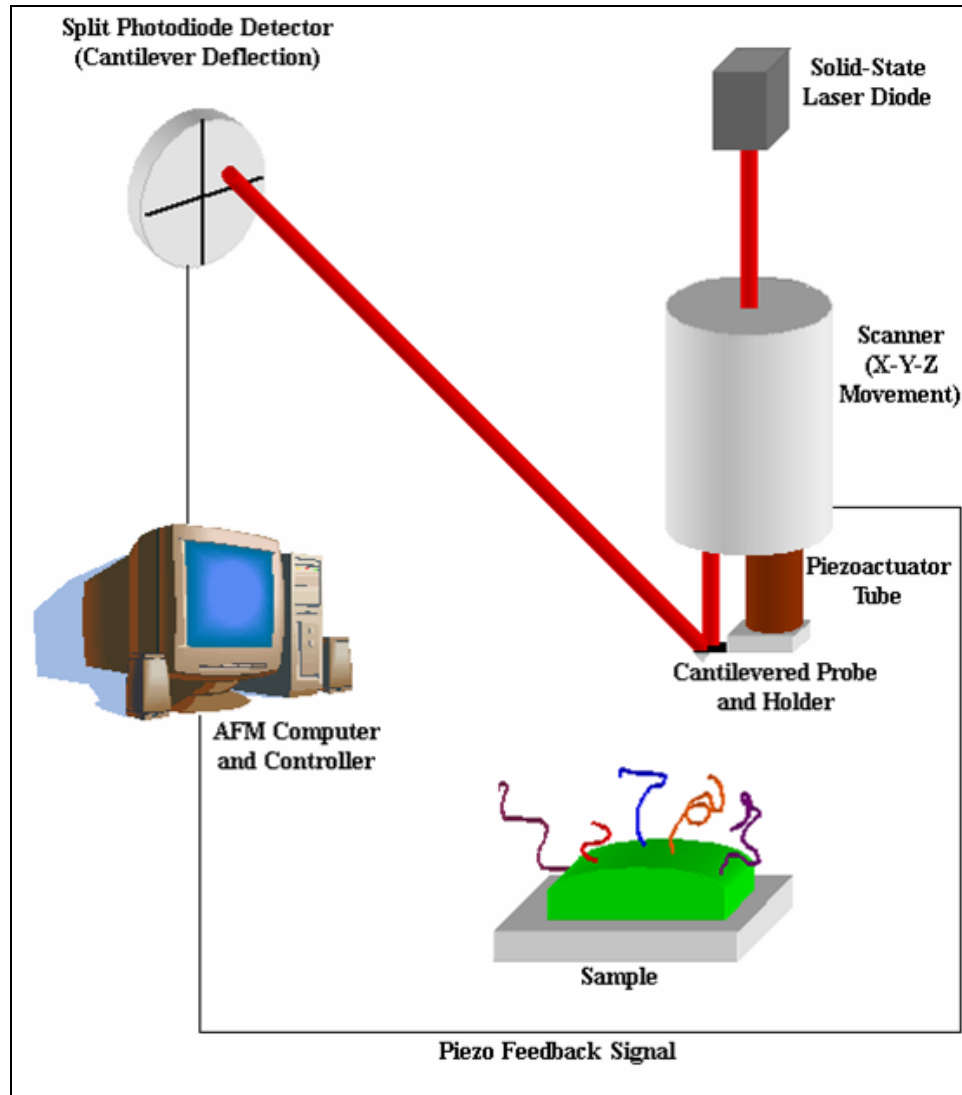
Figure 4 – Schematic diagram of AFM analysis of a bacterial surface. The laser reflects off the gold-coated cantilever, into the photodiode. In TappingMode™, the cantilever is maintained at constant amplitude via a piezoelectric tube. Changes in the angle of the incident light register as potential changes on the photodiode. These data may then be deconvolved into a plot of deflection voltage versus piezo tube position. Adapted from [4].

When operating, the head raster-scans the sample surface. Features on the surface, such as microbial cells, cause changes in the cantilever deflection, altering the input signal to the feedback loop. Depending on the AFM mode (Contact or TappingMode™), the feedback loop is adjusted back to the setpoint by means of a series of gains.

The data collected from the cantilever deflection may also be used to generate plots of deflection voltage versus separation distance. As an example, Figure 5 shows a force cycle for a cantilever interacting with a "cell". Relative cantilever position is noted in both the curve and the inset of the figure.
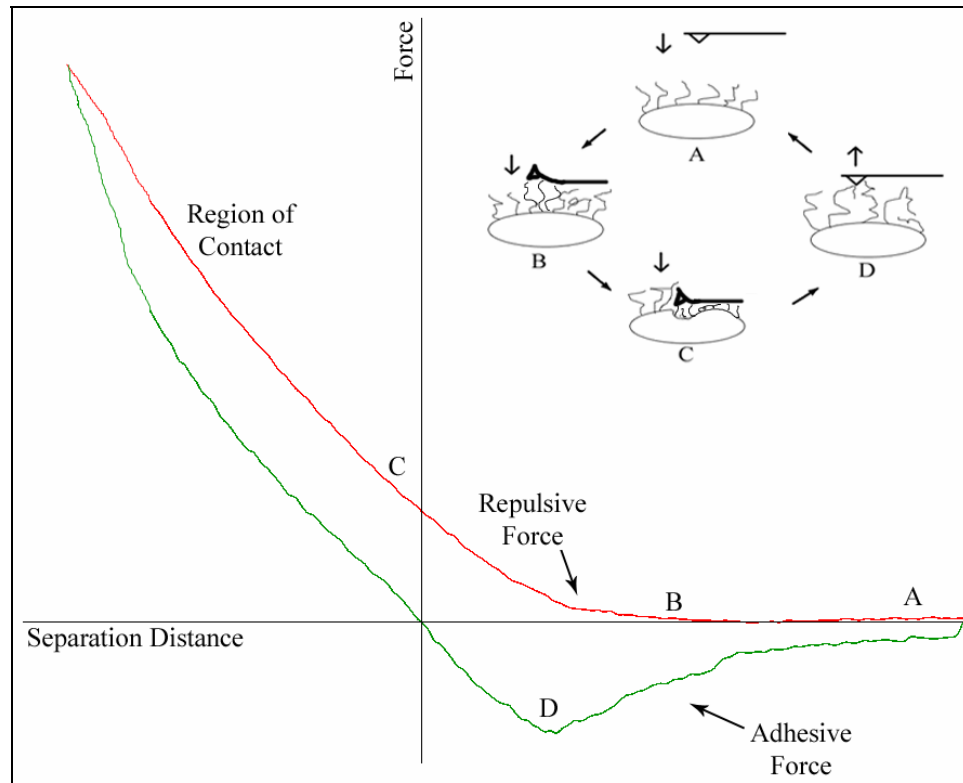
Figure 5 – Schematic of relative cantilever position in a typical force cycle. As the probe approaches the sample (A), it begins to interact with surface structures (B), and eventually contacts and deforms the sample surface (C). As the probe retracts from the sample, other interactions, due to surface structures adhering and breaking off from the cantilever, become evident (D).

At position A, the probe is far from the cell surface, as is indicated by the schematic, and by the lack of any change in force with separation distance in the curve. As the probe comes closer to the cell, however, it begins to interact with the microbial polymer brush and cell wall (Position B). A positive value of force indicates a repulsive interaction, meaning the cantilever is deflected upwards by the physical (cell wall

19

elasticity, polymer rigidity) and/or chemical (electrostatic or steric interactions) properties of the cell. Position C represents the Region of Contact, where the AFM probe and cell wall move at the same velocity as the probe indents the sample surface. As the cantilever is pulled back from the cell surface, it is possible that surface structures have sorbed to the probe during contact. These structures extend from the surface and, at some point in the retraction, detach from the probe. These pull-off events are represented by negative forces (adhesions) in the force cycle.

2.2.2 – Force Curve Analysis

To obtain plots of force versus separation distance, it is necessary to define zero points of both cantilever deflection and scanner position. The method used in this analysis was based on that of Ducker and Senden [31], who examined the interactions of spherical colloidal probes with planar surfaces in liquid media. Figure 6 graphically describes the process of conversion from cantilever deflection-scanner position data to force-separation data.

In Figure 6A, one can see the raw data presented in the cantilever deflection-scanner position plane. The raw data is essentially hanging in space until a coordinate system is defined. This technique follows two criteria: The first is that, at large separation distances, there is no interaction between the sample and the probe (Position A in Figure 5). This allows us to simply translate the curve up and down until it is aligned with the horizontal axis.

The second criterion is that the cantilever shows a linear relationship between deflection and piezoactuator position at high loading forces. This occurs in the constant

compliance region, where cantilever deflection is due solely to the movement of the scanner. By applying the assumption that cantilever deflection changes linearly with the piezoactuator position when the probe is in stiff contact with the sample surface, we expect the constant compliance region of the deflection curve to be vertical, since the sample surface is not deforming in response to the position of the scanner. It is important to note that this method will overestimate the value of force at zero separation distance if the sample is not significantly stiffer than the cantilever [31].

Once the reference points have been defined, it is necessary to qualify the features of the curve, most especially by verifying the presence or absence of attraction (regions of negative deflection) in the approach curve. For purely repulsive curves, the raw deflection plot is simply translated such that the constant compliance and zero interaction regions align with the vertical and horizontal axes, respectively. The presence of attraction, however, requires special treatment, and is a matter of some debate. This will be discussed fully in Section 2.2.2.1, below.
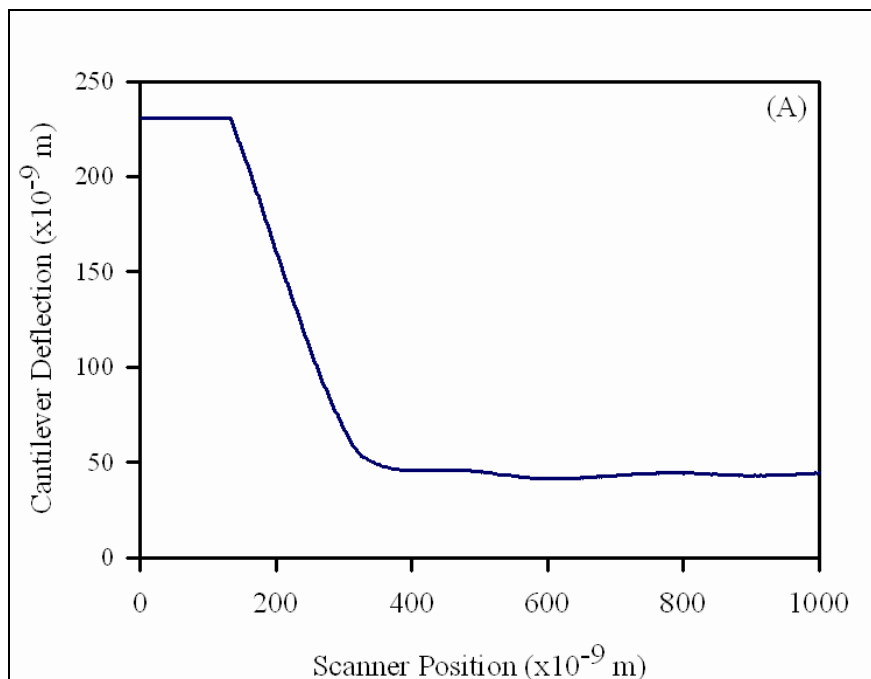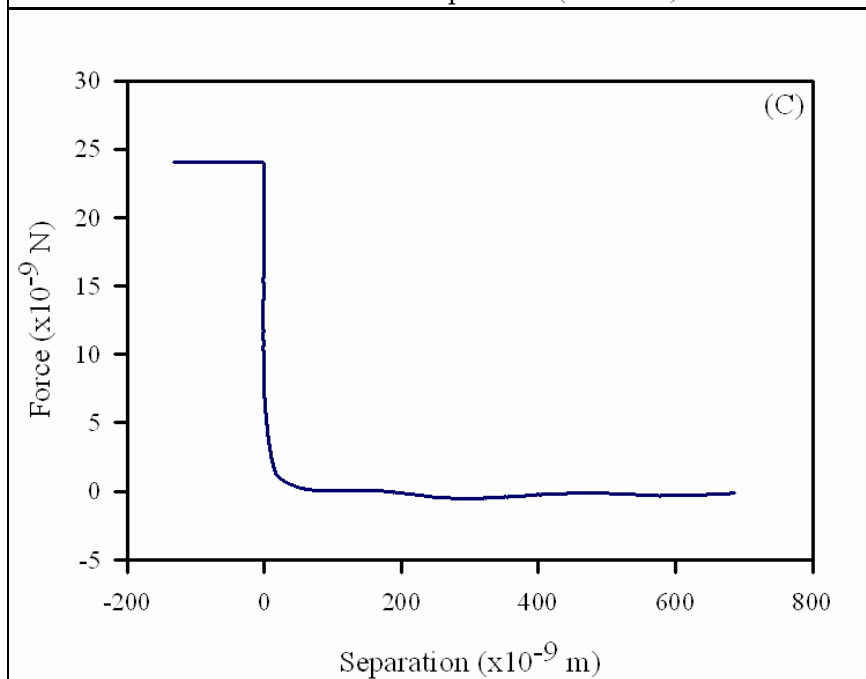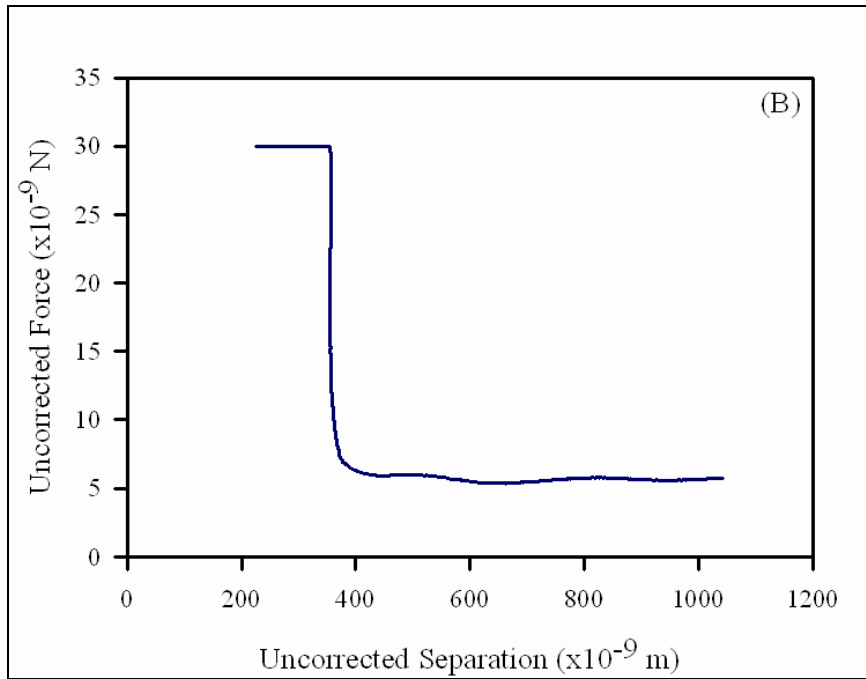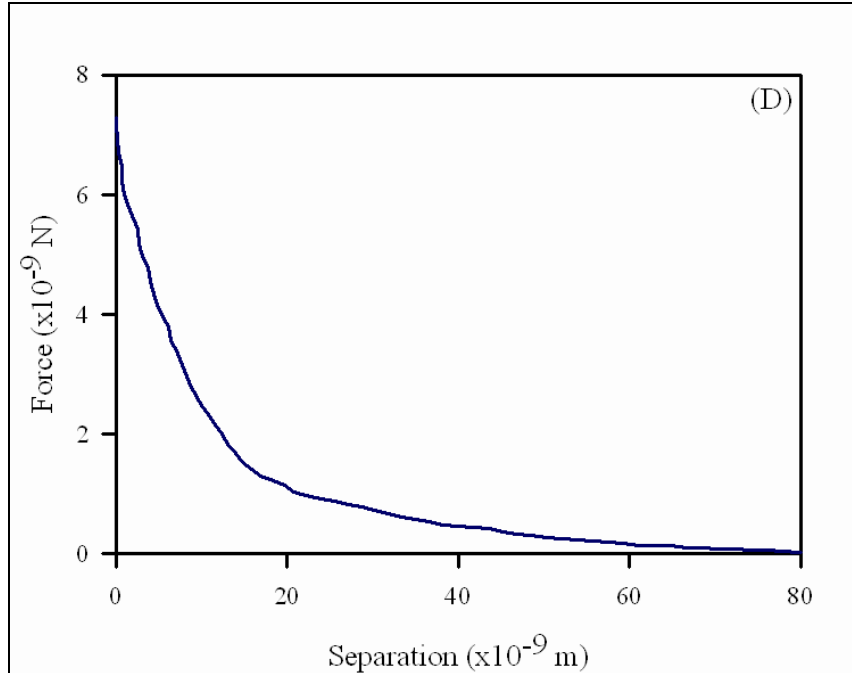
Figure 6 – Illustrations of correcting a force cycle, and transformation from deflection to force data. (A) represents the raw data generated by the AFM. In (B), the deflection data are transformed to force via Hooke's law. The region of contact is made vertical by subtracting the deflection of the cantilever. (C) includes the two offsets in the curve to align the region of contact and the region of zero interaction with the axes of the Cartesian plane. (D) shows the formatted data series in which only positive distances are considered. Adapted from [31].

Deflection data are converted to force via Hooke's Law, which describes a linear relationship between these two quantities via an empirical parameter k, the spring constant of the cantilever.

$$F = -kx \qquad (1)$$

Where F is the interaction force and x is the deflection of the cantilever. Figure 6B shows the corrected force-separation curve. It should be noted that this approximation of cantilever deflection assumes temporal equilibrium, *viz.* that the rate of cantilever deflection does not change with time, and that there is no nonlinear element to the deflection. This may present problems in the case where the cantilever is stiffer than the sample surface, in that deformation of the sample surface by the cantilever may lead

to irregularities as the probe contacts the sample. For the case where the cantilever is much more compliant than the sample, however, this is not an issue. Here, only the cantilever will deform when the probe and sample are in contact, and linearity may be confirmed graphically in the region of high loading force.

2.2.2.1 – Interpretation of AFM Force Curves Including Attraction

AFM force curves may be interpreted in several ways, depending upon the reference points used to define the sample surface and baseline interaction force. For example, Ducker et al. [31] define their coordinate system by aligning raw deflection data to the axes of a Cartesian plane, requiring that the cantilever be significantly more compliant than the sample surface. In the constant compliance region, where the cantilever deflects linearly with piezoactuator position, the probe is in rigid contact with the sample surface. Since we assume that the probe cannot deform the sample surface, cantilever deflection in this region is due solely to piezoactuator movement, allowing us to define the surface by aligning the constant compliance region to the force axis. Contact mechanical models, such as those presented in [18] and the references therein, define the surface mathematically.

In the case of purely repulsive approach interactions, these methods agree in their treatment of the AFM data. When attraction exists in the approach curves, however, contact mechanical models disagree on which point actually represents zero separation. For convenience, this reference is often the relative minimum of the attractive interaction, which represents the point at which all forces acting on the cantilever sum to zero. None of these models, however, explicitly accounts for the presence of a polymer brush. This

becomes a problem in microbiological contexts, where long, heterogeneous brushes are common.

Addition of a polymer brush complicates the process of defining the surface with attraction in the approach curve. After the attractive minimum, the cantilever gradually returns to its rest position, as steric repulsion becomes the dominant tip-sample interaction, and then deflects vertically into the constant compliance region. Probing *C. parapsilosis* with a DNPS cantilever, we see ~65 nm of additional piezoactuator movement between the attractive minimum and the onset of the constant compliance region Figure 13. This suggests that the cantilever is indenting 65 nm into the cell wall before reaching a less compliant surface. The distance between these same two points for silicone rubber and a DNPS cantilever (Figure 15, inset) shows a distance of <1 nm. It is interesting to note that the silicone rubber-DNPS system represents the only system in this study not involving a polymer brush on the probe, the sample, or both. It is also the only system which behaves as contact mechanical models predict.

For systems involving one or more polymer brushes, the method of Ducker et al. is still valid, since a constant compliance region occurs. Contact mechanical models, however, fail to describe the interactions in three important ways: First, aligning the attractive minimum to the force axis leads to an unrealistically high value of the energy required to return the cantilever to its rest position ($> 10^{-17}$ J). Second, it is necessary that the constant compliance regions of the approach and retraction curves overlap, demonstrating a lack of or correction to piezoactuator hysteresis. By analyzing approach curves according to contact mechanical models and recognizing this necessity, several or all of the adhesive interactions in the retraction curve are translated into Quadrant III of

the Cartesian plane. This suggests that the probe is plastically deforming the cell wall, which is highly unlikely. And third, alignment to the attractive minimum suggests that the polymers in the brush are point volumes which may be infinitely compressed. Since we know, according to the Pauli Exclusion Principle [78], that all molecules take up space and cannot exist in the same space at the same time, the contact mechanical models violate a basic physical law in these particular systems. This treatment also eliminates steric interactions, which are known to be dominant for many microbial strains at small separations [7, 21, 103].

Since the repulsive steric forces add to the total force acting on the cantilever, the inclusion of this force causes an outward (positive separation) translation of the "surface" predicted by contact mechanical models. The actual sample surface must therefore exist somewhere below this attractive minimum. It is our argument that, since the constant compliance region is used as the reference point in all systems not involving polymer brushes [18, 31, 81], the same reference should be used for those with polymer brushes, enabling comparison between disparate systems. As such, all force curves in this analysis will be processed according to Ducker et al's method, since this is the more logical standpoint available to defining the sample surface.

2.2.3 – AFM in Biological Systems

The AFM has proven to be a versatile and precise device for the examination of biological systems. Other microscopic techniques, including scanning electron microscopy (SEM), transmission electron microscopy (TEM), and confocal laser scanning microscopy (CLSM), require chemical treatments, metallic coatings, and/or

various degrees of dehydration of the samples to obtain clear images [93]. All of these treatments, however, affect the morphology of biological samples. AFM is capable of operating in a variety of environments, including in liquid media, which allows for the simulation of environmental and physiological conditions. Further, samples do not require chemical preparation prior to examination under the AFM.

Several groups have undertaken projects examining various aspects of biological and microbiological properties using the AFM. Exploiting the device's excellent lateral resolution, the AFM has become an elegant tool for imaging microbial cells and surface structures [32, 42, 98], as well as real-time monitoring of cell morphology changes after treatment with various chemicals [22]. Further, the AFM's force mode may be used to determine nanoscale force interactions between the probe and a cell [47], which may be deconvolved into physicomechanical [44, 96, 98, 99] and physicochemical [7, 21, 97] properties of the cell and its surface structures.

2.2.4 – *In situ* Probe Modifications

While useful for obtaining a great deal of data regarding the properties of cells and specific molecules, the limited variety of probe materials (primarily silicon and silicon nitride) has led to an extension of the AFM using probes modified with different chemicals and biological molecules. Bowen et al [15, 16] were among the first to immobilize single microbial cells on AFM probes, allowing for the quantitative analysis of interactions between different materials and immobilized cells.

Since these first attempts at measuring interactions between two biological surfaces, a number of groups have gone on to examine interactions between single

molecules [53, 58, 95] or whole microbial cells [75, 80, 81] and various surfaces, including biomaterials and microbial biofilms. This research has led to great advances in determining the strength of nanoscale interactions between ligand pairs, as well as quantitatively evaluating the affinity of whole cells for different substrata, including to soil minerals [61, 62] and biomaterials [37, 81].

2.3 – Mathematical Modeling

The data contained in force-distance curves are the product of multiple discrete forces acting simultaneously as the AFM probe and sample interact. Individual contributions of these forces may be modeled mathematically, assuming that these forces are additive. Figure 7 demonstrates this phenomenon of superposed forces (van der Waals, electrostatic and steric interactions) adding to a single observed force-distance interaction.
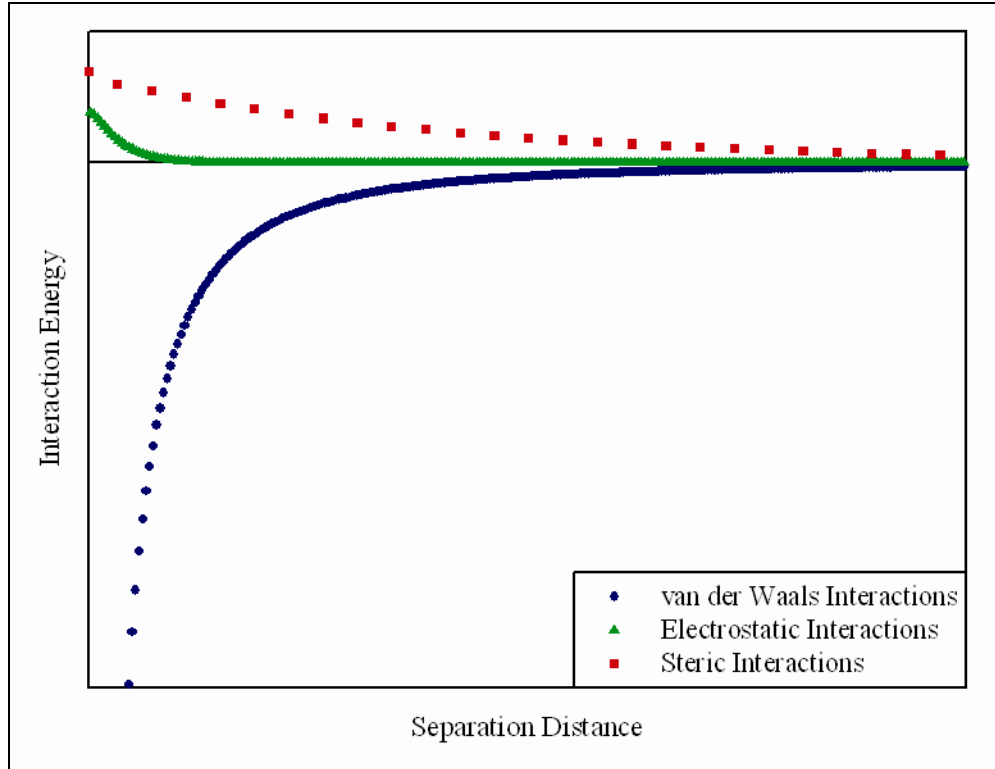
Figure 7 – Example diagram of possible interaction energy contributions to a force-distance curve due to different physicochemical phenomena. It is possible to mathematically discretize the data into its additive components by means of established mathematical theories. Adapted from [21].

Each of these separate forces creates some aspect of the interactions recorded with AFM, and must be separately identified and described before the total interaction is fully understood. In the following sections, we will describe several mathematical models commonly applied to microbiological systems and determine which forces play dominant roles in the interactions of our model microbes with different substrata.

2.3.1 – Colloidal Stability of Small Particles (The DLVO Theory)

Owing to their small size and regular geometries, microbial cells in solution may be described quite accurately by established colloidal theories [6, 21]. As an approximation of the long-range interactions between colloidal particles and flat surfaces, Derjaguin and Landau [29] and Verwey and Overbeek [105] formulated a linearization of the Poisson-Boltzmann equation using the Debye-Hückel approximation (*viz.*, that ions in solution contribute equally within the electrostatic double-layer around two spherical particles). Their separate work led to solvable equations that describe the London-van der Waals and electrostatic interactions between colloidal particles at ranges of tens of nanometers from a particle surface. These two equations together make up the Derjaguin-Landau-Verwey-Overbeek (DLVO) theory of colloid stability.

Assuming a sphere-sphere systemic geometry, and that electrostatic repulsions (E_E) and London-van der Waals attractions (E_V) may be linearly superposed, the generalized expression for the total interaction energy, E_T, is described by Hogg et al. [50] as:

$$E_T = E_E + E_V \qquad (2)$$

Where E_E for the system is given by:

$$E_E = \frac{2\pi a_m a_p N_A}{(a_m + a_p)\kappa^2}\left(\varphi_m^2 + \varphi_p^2\right)\left\{\frac{2\varphi_m\varphi_p}{\varphi_m^2 + \varphi_p^2}\ln\left[\frac{1+\exp(-\kappa h)}{1-\exp(-\kappa h)}\right] - \ln\left[1+\exp(-2\kappa h)\right]\right\} \qquad (3)$$

With a_m and φ_m being the radius and reduced potential of the microbe, respectively, a_p and φ_p the radius of curvature and reduced potential of the cantilever probe, respectively, h the separation distance between the two, and N_A Avogadro's

number. The reduced potentials are functions of the microbial and probe surface

potentials (ψ_m and ψ_p, respectively), following:

$$\varphi_i = \frac{ze\psi_i}{k_B T} \tag{4}$$

Where k_B represents the Boltzmann constant, T the absolute temperature, z the

bulk valence of ionic species, and e the unit charge of a single electron. κ, the Debye

screening length, is defined as:

$$\kappa = \left(\frac{1}{\varepsilon_0 \varepsilon_R k_B T} \sum_{i=1}^{N} z_i^2 e^2 n_{i,\infty} \right)^{1/2} \tag{5}$$

Where ε_0 is the dielectric permittivity of a vacuum, ε_R the relative dielectric

permittivity of water, and $n_{i,\infty}$ the number concentration of ions in solution. This model is

applicable to systems of 1:1 electrolytes with surface potentials less than 60 mV, and

assumes that the surface potentials remain constant throughout the approach [50].

The surface potential of the microbe is assumed equal to its zeta potential [86], as

calculated from experimental values of electrophoretic mobility and the Smoluchowski

Equation (6) [108].

$$\mu_E = \frac{\varepsilon_0 \varepsilon_R \zeta_{Smol}}{\mu_f} \tag{6}$$

Where μ_E refers to the sample's electrophoretic mobility, ζ_{Smol} the zeta potential

and μ_f the fluid viscosity, taken as that of water.

London-van der Waals interactions between colloidal particles were described by

Hamaker [43] in 1937. Further study showed that, at distances greater than a few

nanometers, the electromagnetic nature of the interactions had a retarding effect on their

magnitude. Gregory [40] described an approximation, based on the work of Overbeek

[76] and Casimir and Polder [23], to account for the retarded interactions between a sphere (the AFM probe) and a flat plate (the microbial cell).

$$E_V = -\frac{Aa_m a_p}{6h(a_m + a_p)\left(1 + \frac{14h}{\lambda_C}\right)} \tag{7}$$

Where a_i and h are defined as before, A is the Hamaker constant describing the van der Waals interactions between the probe, surface and surrounding media, and λ_C is the "characteristic wavelength" of the interaction, whose value is often taken as 100 nm [40]. The term $\left(1 + \frac{14h}{\lambda_c}\right)$ is an empirical correction factor, adapted from the work of Schenkel and Kitchener [86], accounting for retardation effects at short distances ($0 < h < \lambda_c/\pi$ (31.83 nm) and $h \ll a_p$).

A plot of the total interaction energy and its components against separation distance provides a profile describing the approach of one spherical component to another. This is applicable both to modeling a system of a cantilever approaching an immobilized cell, or a planktonic cell approaching a biomaterial or biofilm surface.

Calculation of the Hamaker constant, for use in Equation (7) may be related to contact angles on microbial lawns through the van Oss-Chaudhury-Good equation [100-102]:

$$(1 + \cos\theta_L)\gamma_L = 2\left(\sqrt{\gamma_M^{LB}\gamma_L^{LW}} + \sqrt{\gamma_M^+\gamma_L^-} + \sqrt{\gamma_M^-\gamma_L^+}\right) \tag{8}$$

In this equation, θ_L is the contact angle under liquid L, γ_L the total free energy of the liquid, γ_i^{LW} the apolar (Lifshitz-van der Waals) component of the surface free energy, γ_i^+ the electron-accepting component of the polar (Acid-Base) surface free energy and

γ_i^- the electron-donating component of the polar surface free energy, where M denotes the microbe and L the liquid. Values of γ_L for a number of liquids have been tabulated [90], and values for water, formamide and diiodomethane were taken for calculation of the microbial free energy components. Knowledge of the surface free energy allows us to calculate the Hamaker constant for each microbe, which may be used to calculate their individual interaction energies.

van Oss et al. formulated an algebraic method of determining the Hamaker constant based on the apolar component of the microbial surface free energy [101]:

$$A = 24\pi l_0^2 \gamma_M^{LW} \tag{9}$$

With l_0 being the minimum separation distance between the two contacting bodies. From further work, van Oss determined that the minimum separation distance fell within a range of 1.57 ± 0.09 Å, reducing Equation (9) to the Hamaker constant being equal to the product of the constant terms (1.8585×10^{-18} m^2) and the apolar surface free energy component.

2.3.2 – Colloidal Stability of Small, Soft Particles (The Soft DLVO Theory)

Recent work has shown that the Smoluchowski formulation of electrophoretic mobility overestimates zeta potentials for soft materials, such as bacterial cells [12, 45, 74]. As such, we will compare the results from classical DLVO theory to the so-called soft-particle DLVO theory, developed by Ohshima, which takes into account the ionic strength of the bulk phase and the softness of the particles in solution.

The Ohshima model describes the approximate mobility of soft particles as [12, 74, 94]:

$$\mu_E = \frac{\varepsilon_0 \varepsilon_R}{\mu_f} \frac{\Psi_0/K_m + \Psi_{DON}/\lambda}{1/K_m + 1/\lambda} + \frac{eZN}{\mu_f \lambda^2} \qquad (10)$$

Where Ψ_0 represents the surface zeta potential, Ψ_{DON} the Donnan potential of the polymer layer, K_m the Debye-Hückel parameter, Z the valence of ions in the polymers, N the density of charged groups, and λ a softness parameter with units of inverse length. The parameters Ψ_0, Ψ_{DON} and K_m are all functions of ionic strength, shown by [45]:

$$\Psi_0 = \frac{k_B T}{ze} \left(\ln \left\{ \frac{ZN}{2zn} + \left[\left(\frac{ZN}{2zn} \right)^2 + 1 \right]^{1/2} \right\} + \frac{2zn}{ZN} \left\{ 1 - \left[\left(\frac{ZN}{2zn} \right)^2 + 1 \right]^{1/2} \right\} \right) \qquad (11)$$

$$\Psi_{DON} = \frac{k_B T}{ze} \ln \left\{ \frac{ZN}{2zn} + \left[\left(\frac{ZN}{2zn} \right)^2 + 1 \right]^{1/2} \right\} \qquad (12)$$

$$K_M = \kappa \left[1 + \left(\frac{ZN}{2zn} \right)^2 \right]^{1/4} \qquad (13)$$

Where z_i represents the valence of each ionic species in solution, n the bulk concentration of ions, and $n_{i,\infty}$ the number concentration of ions in solution. The grouped parameter ZN represents the spatial charge density in the polyelectrolyte region.

This system of equations may be solved by the regression of a plot of calculated versus experimental electrophoretic mobility, with fitting parameters ZN and $1/\lambda$. Parameters were varied such that the regression yielded a straight line with a slope of unity and an intercept passing through the origin.

2.3.2.1 – Limitations to Classical and Soft DLVO Theories

While able, in many cases, to describe the interactions between colloids and surfaces, classical and soft-particle DLVO theories do not account for forces other than van der Waals attractions and electrostatic repulsions. Other forces, including steric interactions, specific ion interactions, hydration pressure, non-charge transfer Lewis acid-base interactions, hydration forces, hydrogen bonding, and hydration effects may also play roles in the energetic profiles derived from experiments [83, 101]. Further, Böstrom et al have showed that DLVO theory, as well as many of its extensions, cannot characterize systems at biological salt concentrations [14]. This is due to the inherent assumption that all interactions may be linearly superposed to a total energy profile, and the fact that electrostatic interactions are highly screened at physiological conditions. To fully characterize the interactions taking place experimentally, it is necessary to identify and account for all possible terms in mathematical expressions.

2.3.3 – Steric Interactions with the Microbial Polymer Brush

In many cases, the DLVO theories insufficiently describe systems of small particles, especially if the particles are coated with polymer brushes. This is because DLVO theory inherently assumes that the particles under examination are perfectly smooth, with no asperities or surface structures. In the case of a particle with a polymer brush extending outward into the bulk phase, the steric force becomes important. This force arises from contact between the probe and the polymer brush, where, as the probe pushes down on the brush, the polymers are forced into a more compact spatial arrangement. This reduces the conformational freedom of the polymers in contact with

the probe, leading to a net negative loss in entropy. This loss manifests as repulsion exerted by the polymer brush as the bonds in each polymer are deformed. If both the probe and thee sample surface are coated with polymers, additional steric interactions may arise from contact between the two brushes. The total steric force is dependent upon the polymer surface coverage and brush thickness. In microbiology, where most cells are coated with thick, dense polymer brushes, the steric force is often the dominant interaction in force-distance curves.

A steric model of the force per unit area experienced by two interacting surfaces, one with a grafted polymer brush and the other bare, was developed by Alexander [8] and de Gennes [28], and modified by Butt et al. [19] to describe the interactions between an AFM probe and a polymer brush.

$$F_{St} = 50 k_B T a_p L \Gamma^{3/2} e^{-2\pi d/L} \tag{14}$$

Where F_{St} is the total force due to steric interactions integrated across the surface of a hemispherical probe, L the equilibrium polymer brush length, a_p tip radius of curvature, and Γ grafted polymer density. L and Γ serve as fitting parameters for the model.

This model assumes the total force may be approximated by integrating the force over the entire surface of the probe, which is modeled as a sphere with radius of curvature equal to 250 nm [21]. Using nonlinear regression software, the model may be fitted to the recorded approach curves.

2.3.4 – Cell Wall Elasticity from AFM Force Curves

AFM force curves may also be examined to determine the elasticity (*viz.* the Young's modulus) of the sample surfaces. This has been shown for microbial systems by Touhami and Dufrêne [96] using Hertzian contact models [49, 90]. This quantity is of interest as it provides insight into the nanomechanical behavior of the cell wall. Further, the models used to determine the elasticity may be extended to model attractive behavior seen in AFM force curves and predict the magnitude of these attractions on different substrata.

Two equations which model the loading force of a non-deformable indenter (in this case, the silicon nitride AFM probe) and an infinitely-deformable elastic sample (the microbial cell wall) as a function of indentation depth (δ) have been developed for two different AFM probe geometries. The first, shown in Equation (15), is valid for a conical probe, while Equation (16) describes paraboloid geometry.

$$F_{cone} = \frac{2}{\pi}\tan(\alpha)E^*\delta^2 \tag{15}$$

$$F_{Para} = \frac{4}{3}E^*a_p^{1/2}\delta^{3/2} \tag{16}$$

Where α is the half-opening angle of the tip in radians, and a_p the radius of curvature of the indenter. The indentation depth, δ, is defined as the difference in cantilever deflection between a soft sample (e.g. a microbial cell) and a rigid sample (e.g. mica or glass) as a function of scanner position. By subtracting the values from the soft sample from the rigid sample, one may generate a plot of cantilever indentation versus sample height.

The quantity E^* is known as the surface elastic constant, and is a function of the Young's modulus (E) and Poisson's ratio (v) of the sample material, described by:

$$E^* = \frac{E}{1-v^2}$$
(17)

For biological samples, Poisson's ratio was assumed to be 0.5 [96], and the value for the half-opening angle was taken as 35° from the manufacturer's specification [3].

3 – Materials and Methods

3.1 – Microbial Growth and Storage

Freeze-dried samples of *C. parapsilosis* (ATCC 90018) and *P. aeruginosa* (ATCC 10145) were acquired from the American Type Culture Collection (Manassas, VA, USA). *C. parapsilosis* was maintained on Sabouraud's Dextrose Agar (Emmons' Modification) (Sigma) plates, and grown in Complete Liquid Media (2% w/v peptone, 1% w/v yeast extract, 2% w/v glycerol (Sigma) in distilled, deionized water [ddH$_2$O]). *P. aeruginosa* was maintained on Tryptic Soy Agar (Sigma) plates, and grown in Tryptic Soy Broth (Sigma). All plates were recultured every 14 days. Cells were incubated for 12 hours at 25^oC on a radially oriented tube-rotator (Glas-Col) in 25 mL vented tissue culture flasks (VWR) at approximately 75 RPM. Cells were then transferred to 50 mL of their respective liquid growth media and grown in an orbital shaker bath (Lab-Line) at 37^oC and 160 RPM until late exponential growth phase (Optical density at 600 nm [O.D.$_{600}$] = 0.5 ± 0.05).

3.2 – Cell Morphology, Force Interactions and Cantilever Treatment

Cell cultures were examined with a Dimension 3100 atomic force microscope with Nanoscope IIIa controller (Digital Instruments, Santa Barbara, CA) to establish cell morphology and record interaction forces with silicon nitride cantilever tips (DNPS-type, Digital Instruments) with spring constants of 0.13 ± 0.02 N·m^{-1} (short, thin cantilevers) [21] or 0.25 ± 0.01 N·m^{-1} (short, fat cantilevers) [103]. Cantilevers were placed tips-up in the bottom half of clean Petri dishes and left under UV light for 5 minutes to remove any adsorbed water and/or hydrocarbons.

To immobilize the cells for examination, the cells were bound to cleaned glass slides [21] by first coating the slides with poly-L-lysine (Sigma). In a Petri dish, 1 mL of poly-L-lysine was pipetted over each slide and placed in a laminar flow hood to dry for 10 minutes. While the slides dried, 30 mL of cell culture was divided between 2 centrifuge tubes and wrapped in Parafilm™ to prevent leakage. Tubes were centrifuged at 3000 RPM for 15 minutes, after which time the supernatant was eluted and replaced with a like volume of 0.1 M 2-N-Morpholinoethanesulfonic acid (MES) buffer (Aldrich) at pH = 7.1. Tubes were vortexed to break up the cell pellets, and the contents were poured over the dry glass slides. The Petri dish was then covered and placed on a shaker table for 20 minutes to allow the cells to adhere.

After 20 minutes, the slides were placed on filter paper to remove excess liquid. Slides were affixed to the AFM stage using double-sided carbon tape, and the AFM was configured for TappingMode™ in liquid per the manufacturer's instructions. AFM images were captured for each cell found, and five force cycles per cell were recorded with drive amplitude set to zero (approximating contact mode) for analysis.

Approximately the same point on each cell surface was chosen for comparison between cells. This was accomplished by imaging the cells in TappingMode™ and choosing a point midway down the length of the cell at the crest of the cell surface [104].

Cells were attached to the undersides of the cantilevers using 1-hexadecanethiol (HDT). This chemical has been used extensively in attaching cells to different substrata, since it readily forms a self-assembled monolayer (SAM) on a variety of glasslike and metal substrata [60, 70]. The HDT is dissolved in reagent-grant ethanol, and, as the ethanol evaporates, the molecules orient such that the thiol moiety forms a covalent disulfide linkage to the cantilever surface, and the alkyl chain extends into solution. Microbial cells, which carry a negative net charge under physiological conditions, will therefore possess charged carbonyl and hydroxyl groups. When these groups contact the orient alkyl chain of the HDT, a covalent ester bond is formed, anchoring the cells to the substrate.

Cantilevers were placed under ultraviolet light for 30 seconds to remove any adsorbed water and hydrocarbons, which may be present from the manufacturing process. Cantilevers were held in forceps and sonicated for 1 minute in ddH$_2$O, followed by sonication for 1 minute in reagent grade ethanol (Aldrich). They were then placed tips-up on a clean glass microscope slide. 50 μL of 1-hexadecanethiol (HDT) stock solution (10 mM in reagent-grade ethanol) was then delivered via pipette to cover the tips.

3.3 – Cell Probe Preparation

Attachment of a single *C. parapsilosis* cell to an AFM cantilever was accomplished using a custom-designed micromanipulator with extension arm (stages

from Edmund Industrial Optics, Barrington, NJ). The unit was capable of translating in three axes with 1-micron accuracy. A single silicon nitride chip, with two triangular cantilevers, was attached to the extension arm using double-sided tape. 25 μL of cell culture at a density of 1×10^{11} cells·mL^{-1} was delivered via pipette to a channel of comparable volume etched into a PTFE block. The cantilever was oriented over the cell culture droplet such that both the tips on the cantilever and the droplet were simultaneously visible under a stereoscope (SMZ-10A, Nikon). The cantilever was then moved vertically downwards to the droplet surface until the tips were submerged, and left for 5 minutes to allow cell adhesion to the HDT SAM. Chemically, any carboxyl groups on the cell surface will bind to the alkyl end of the HDT, forming a covalent ester linkage.

The cantilever was carefully withdrawn from the droplet, dried for 5 minutes in a laminar flow hood, and viewed with an optical microscope (Eclipse E400, Nikon) equipped with an ultraviolet ($\lambda = 330 - 380$ nm) filter cube to verify attachment. *C. parapsilosis* is weakly autofluorescent in UV wavelengths, eliminating the need for chemical staining to verify attachment. We found that using the short, fat cantilever gave the best reproducibility in immobilizing the cells.

3.4 – Scanning Electron Microscopy

In order to verify cell adhesion and orientation on the cantilevers, six cellular probes were prepared for analysis with a scanning electron microscope (Amray 1610 Turbo, Bedford, MA). After treatment, cantilever chips were placed in a desiccator for four days to dehydrate the chemisorbed cells. They were then mounted on an SEM

sample holder with carbon tape and placed in a Desk II Cold Sputtercoater (Denton Vacuum, Moorestown, NJ) and coated for 20 seconds at 45 mA. Gold-coating of the samples is necessary to increase overall sample electron density, making the cells visible to the electron beam.

After coating, the samples were placed in the SEM chamber, which was then closed and evacuated. The SEM was calibrated at an acceleration potential of 20 kV, and each intact cantilever was examined at four points (each cantilever leg, the base between the legs, and the tip) for the presence of bound cells. Images were captured for each cell, at magnifications of 5.0 kX to 15.0 kX.

It should be noted that this experiment was done only to verify that cells adhered, and determine where they would do so. Since the cells were not chemically fixed prior to desiccation in this experimentation, we expected morphological changes as the cells dried.

3.5 – Approach Interactions at the Cell-Biomaterial Interface

With the spore probes prepared, it was now possible to measure the interactions between a biomaterial surface and the probe. Silicone rubber, a common implant material, was chosen for this study. Medical-grade silicone rubber tubing (VWR, 0.25" I.D.) was cut with sterile scissors to approximately 1 inch in length, and then sliced to allow access to the inner luminal surface. The section of silicone was then taped flat to the bottom half of a Petri dish to prevent curling. A 2 cm^2 area of silicone in the center of the dish was sufficiently flat for examination with the AFM. With a cell probe mounted in the AFM fluid cell, we manually focused the AFM optics on the sample surface.

When the fluid cell was approximately 2 mm from the sample surface, MES buffer (pH = 7.1) was delivered via pipette until the cell probe was covered.

After setting software parameters according to the manufacturer's instructions for TappingMode™ in liquid, the AFM was engaged. Force cycles were recorded for 8 - 10 different areas with 3 data sets taken on each area. Biomaterials were also examined using an unmodified probe to compare with cell probe data, and surface roughness data were recorded to examine local surface features that could affect cell adhesion. Further, the biomaterials were examined using a probe coated with HDT only, to serve as a control for the effect of HDT-coated probes on probe-biomaterial interactions. In order to compare the affinities for each substrate (a bare probe with a cell bound to glass, and a functionalized probe on bare silicone and on a biofilm grown for three days on silicone), the retraction portion of each force cycle was processed. The magnitudes of the pull-off forces show the relative strengths of binding to each substrate after contact.

3.6 – Approach Interactions at the Cell-Biofilm Interface

As an extension to the experimentation in section 3.5, it was now of interest to characterize the interactions between spore probes and biofilms grown on silicone rubber. The parallel plate flow cell (Model FC-71, BioSurface Technologies Corporation, Bozeman, MT) (Figure 8) was opened and cleaned, after which a coupon of silicone rubber was fixed into the channel with double-sided tape.
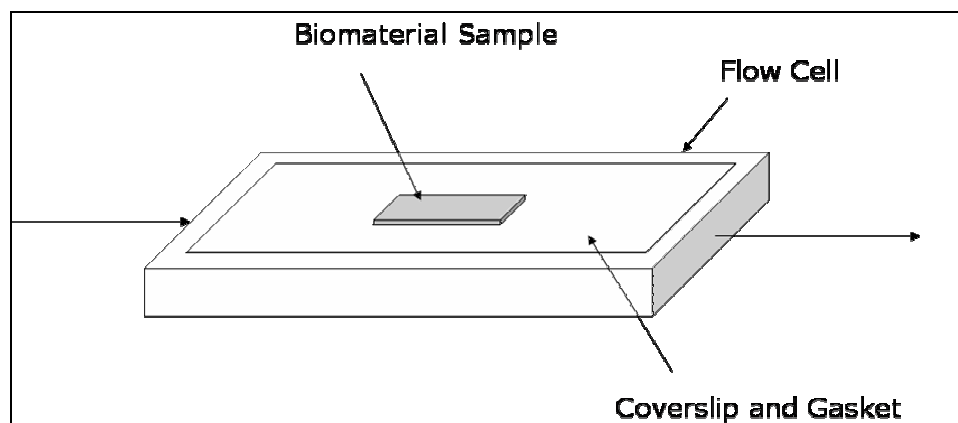
Figure 8 – Schematic of the parallel-plate flow chamber used for biofilm formation. A channel etched into the base allows for placement of a biomaterial coupon inside the chamber without disrupting flow. Shear effects were minimized by setting the fluid velocity to 380 cm·min^{-1}, which correlates to Re ≈ 200.
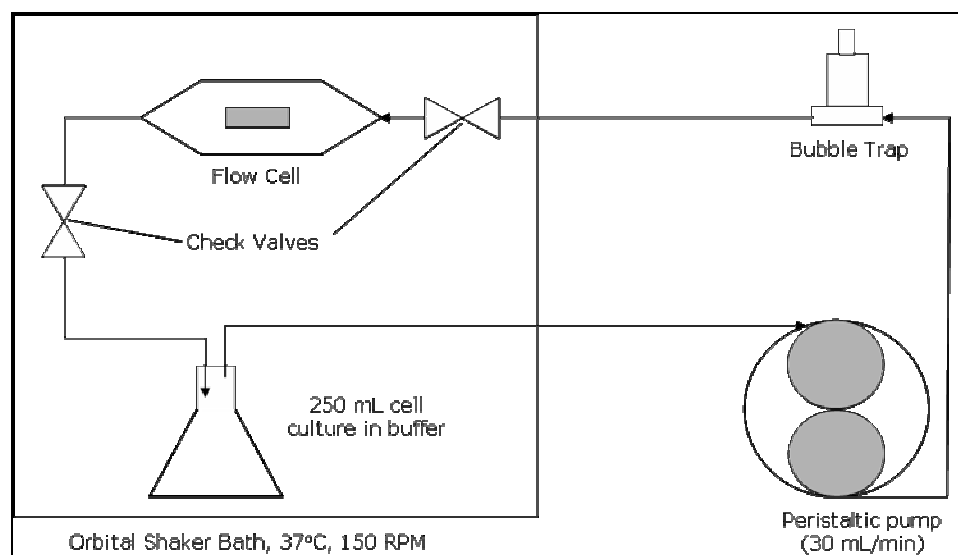
Figure 9 – Schematic of the fluid circuit used to grow biofilms. The circuit is maintained at 37°C to emulate *in vivo* conditions. Bacteria are suspended in MES buffer with no growth factors, allowing for examination of the initial events in biofilm formation.

The rubber was pressed gently with tweezers to ensure adhesion to the tape. A standard #2 (24 x 60 mm) microscope cover slip was then placed over the channel, followed by the flow cell gasket. The flow cell cover was then replaced, and screws were tightened to two full turns of their final position. 0.125" I.D. silicone rubber tubing was fitted over the two access ports and secured with cable ties. Check valves were then

placed in-line, and the entire unit was autoclaved at 121°C for 20 minutes to sterilize. After cooling, the screws were tightened to prevent leakage during the experiment. The flow cell was held in a custom support brace inside the shaker bath cover and secured with silicone screws. The check valves were then connected to the feed and drain lines for the fluid circuit.

A 60 mL sample of *P. aeruginosa* (O.D.$_{600} \cong 0.5$) was divided into four 15 mL centrifuge tubes, wrapping the caps in Parafilm™ to prevent leaks. The tubes were centrifuged at 3000 RPM for 15 minutes (25°C), after which time the supernatant was eluted and replaced by a like volume of 0.1 M MES buffer (pH = 7.1). The tubes were re-sealed, vortexed to disperse the cell pellet, and then added to a 250 mL flask of MES buffer. Additional MES buffer was added to the flask to bring the final volume in the flask to 250 mL. This flask served as a bacterial reservoir for use in the fluid circuit, shown in Figure 9.

The peristaltic pump (Manostat "Vera" Varistaltic Pump, Fisher Scientific) was fitted with 0.25" I.D. silicone rubber tubing and set to speed 4. This corresponds to a fluid velocity of 94.75 cm·min^{-1}, or a fluid Reynolds number of approximately 100. This minimizes the effect of shear on the nascent biofilm while still allowing the pump to operate in a non-pulsatile regime. The fluid circuit was maintained at 37°C in an orbital shaker bath (Lab-Line), with minimal heat loss by convection in the tubing outside the bath. Cells were kept in suspension in the flask by agitation at 160 RPM. A bubble trap was installed in the feed line to damp potentially pulsatile behavior caused by the peristaltic pump. The tubing was necked to 0.125" I.D. before the bubble trap for connection to the other units in the circuit. This increases the fluid velocity to 380

cm·min^{-1}, corresponding to a Reynolds number of about 200. The final level of fluid in the flask was recorded at the beginning of experimentation and checked hourly to verify that the circuit was not leaking. All connections in the circuit were secured with cable ties and wrapped with Parafilm™ to prevent leakage.

Biofilms were allowed to grow for 1 or 3 days in the flow cell. After this time, the pump was stopped and the check valves disconnected to maintain hydration of the biomaterial sample. The flow cell was then removed from the circuit and brought to the AFM, where the screws, cover, gasket and microscope coverslip were carefully removed. With a reserve of MES buffer at hand to periodically replenish any evaporating liquid, the AFM was configured with a modified cantilever and operated as before. The procedure was repeated with an unmodified cantilever for comparison. Cantilevers used in this experimentation were the short, fat cantilevers, having a nominal spring constant of 0.25 ± 0.01 N·m^{-1} [103].

3.7 – Electrophoretic Mobility Analysis

In order to characterize the interaction energy profiles of the two model microbes, it was necessary to determine their surface potentials as a function of solution ionic strength. This quantity, taken as equal to the zeta potential of the microbes, for convenience, may be related to the microbial electrophoretic mobility by Equation (6), or, if the microbes are considered soft, by Equation (10). The electrophoretic mobilities and surface potentials of both *C. parapsilosis* and *P. aeruginosa* were measured using a zeta potential analyzer (Zeta PALS, Brookhaven, Holtsville, NY). Mid-exponential growth phase cultures were centrifuged at 3000 RPM and resuspended in MES buffer (25°C, pH

= 7.1). Measurements were taken as a function of buffer ionic strength (Deionized water [I.S. ≈ 1 x 10^{-6} M], 0.02, 0.04, 0.06, 0.08, and 0.1 M). All measurements were recorded four times and averaged.

3.8 – Microbial Interaction Energy Analysis

In order to determine the contribution of London-van der Waals forces to the interaction energy profiles, it is necessary to determine the Hamaker constant describing the microbe-AFM probe-fluid system. Being a function of the free energy components of the microbes, we may obtain the Hamaker constant by measuring the contact angles of microbial lawns under various liquids. Contact angles were recorded for both microbes under the three liquids of interest using a Rame-Hart NRL Contact Angle Goniometer (Model #100, Mountain Lakes, NJ) with 80 readings taken on both sides of each liquid droplet and averaged. Using Equation (8) and the contact angle data, we may solve three instances of the equation simultaneously to return values for the three surface free energy components (γ_M^{LW}, γ_M^+ and γ_M^-). We may then calculate the Hamaker constant from Equation (9), and the contribution of London-van der Waals interactions to the final energy profile by Equation (7).

4 – Experimental Results

4.1 – Microbial Growth Curves

Growth curves for *P. aeruginosa* and *C. parapsilosis* are shown in Figure 10 and Figure 11, respectively. The absorbance data obtained were fitted using an exponential regression, since cells must be harvested from culture in the mid- to late-exponential

phase of growth. Assuming a first-order logarithmic relationship between absorbance and cell growth, the form of this regression will follow the equation:

$$A_m = A_0 \exp(\mu t) \tag{18}$$

Where A_m is the measured optical density of the culture, A_0 is the optical density at time = 0 hrs, t is elapsed time, and μ is the specific growth rate, which is obtained from the regression.
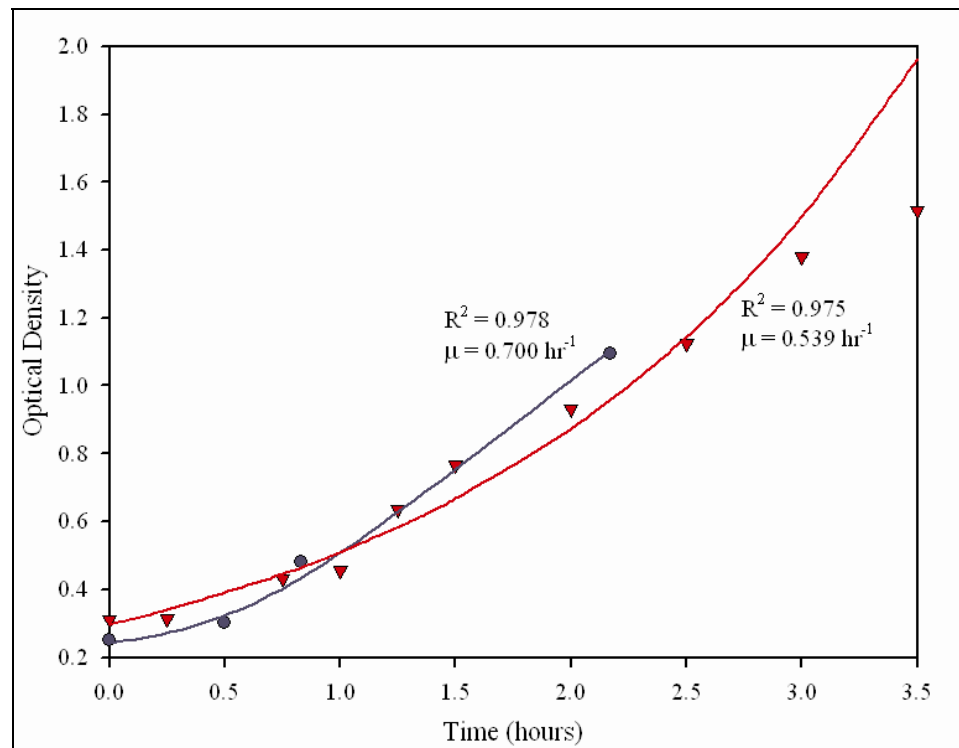
Figure 10 – Growth curves and exponential regressions for *P. aeruginosa*. Different data sets represent duplicate experiments at the same experimental conditions.
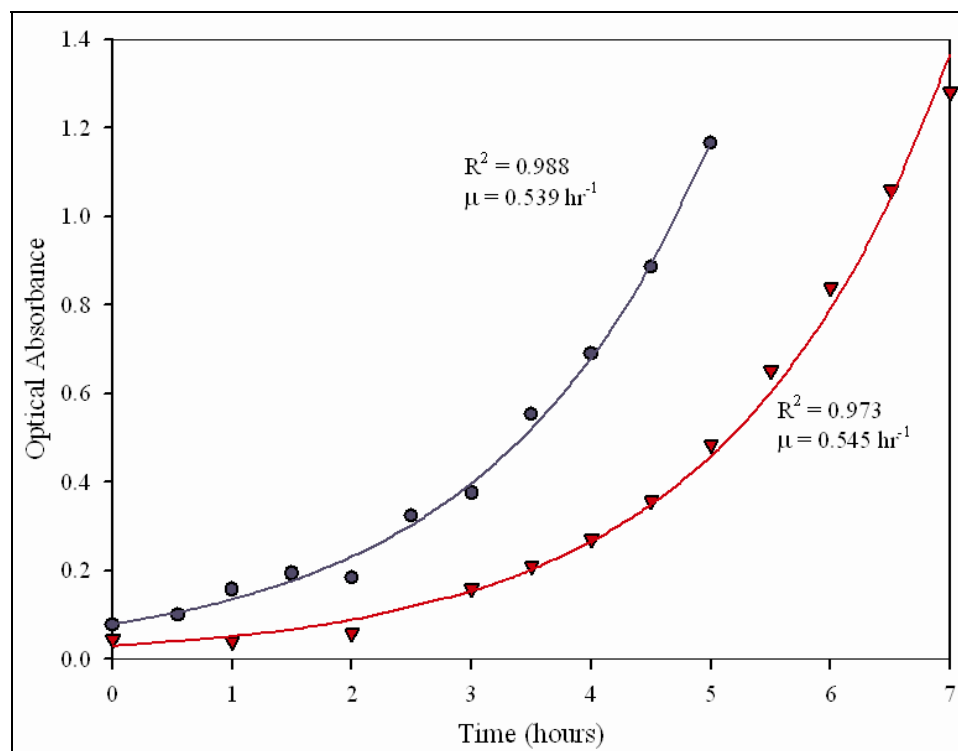
Figure 11 – Growth curves and exponential regressions for *C. parapsilosis*. Different data sets represent duplicate experiments at the same experimental conditions.

4.2 – Cell Morphologies and Example Force Cycles

P. aeruginosa cells are rod-shaped, 2 - 3 μm long and ~1 μm in diameter (Figure 2). Measurements of the forces between the unmodified silicon nitride probe and individual cells of *P. aeruginosa* during the approach of the probe to the cell show interactions beginning at 70 nm from the cell surface (Figure 12). Only repulsive interactions exist for this cell during the approach portions of the force cycle, and reach a maximum value of 5 - 7 nN at the point of zero separation.

Morphologically, *C. parapsilosis* cells are spherical, with diameters of 4 - 6 μm (Figure 3). The approach curves describing the interactions between an unmodified silicon nitride probe and individual cells of *C. parapsilosis* are shown in Figure 13.

49

Interactions start at ~80 nm from the cell surface, with a characteristic adhesion of 0.9 ±

0.4 nN at 55 nm, with a 6 nN repulsion at the cell surface.
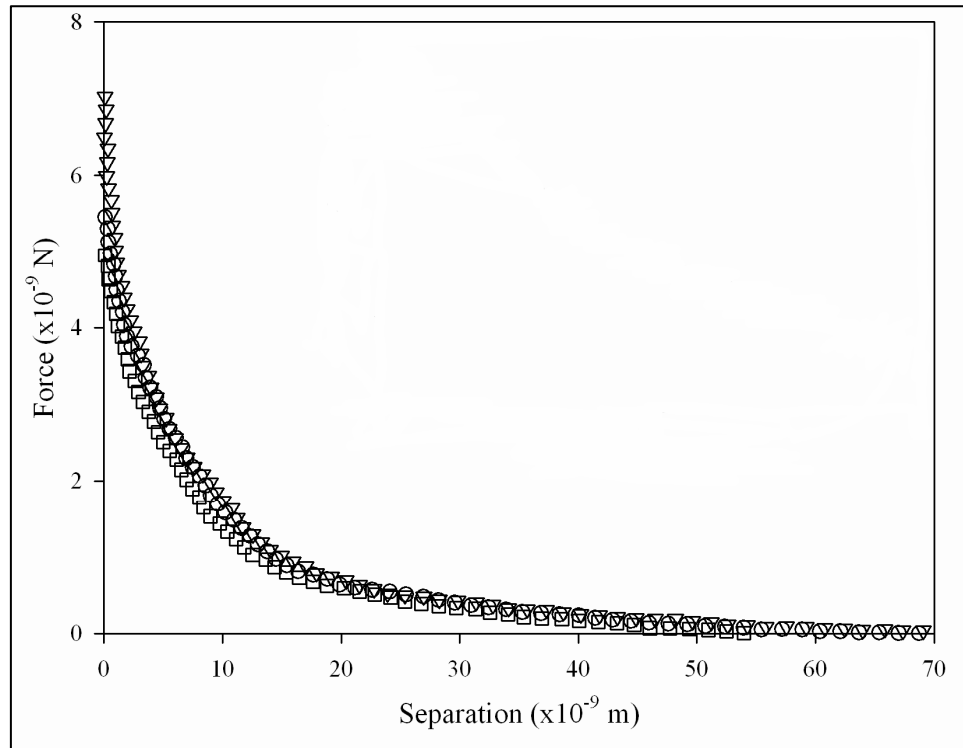
Figure 12 – *P. aeruginosa* approach curves with unmodified silicon nitride probe – Data shown represents five measurements on a single cell with the average of the five also plotted. Interactions begin at 70 nm from the cell surface, and are purely repulsive in nature. Repulsion at zero separation distance reaches a value of 6.0 ± 1 nN.
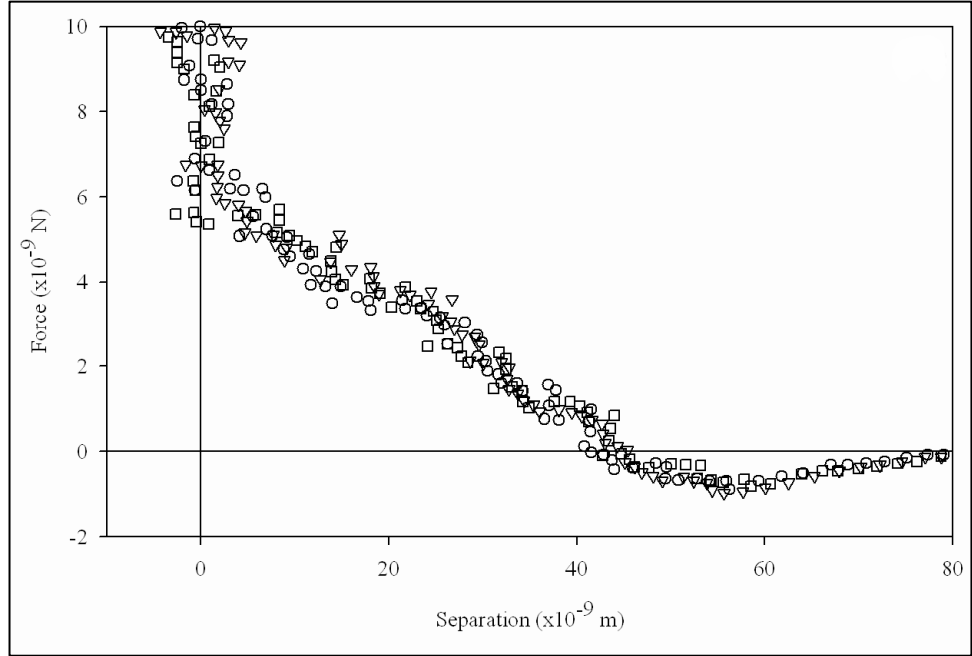
Figure 13 – *C. parapsilosis* approach curves with unmodified silicon nitride probe – Data shown represents three measurements on a single cell. An attractive interaction begins at approximately 80 nm from the cell surface, with a final magnitude 1 nN at 55 nm from the cell surface. After this point, surface polymers become more important than the attraction, leading to a steric repulsion of ~6 nN at the cell surface.

4.3 – Cell Probe Preparation and SEM Analysis

After preparation of the cellular probes, we verified adhesion and placement of the cells on the cantilevers. Examination of the cellular probes with SEM showed cells bound to the cantilever with multiple cells present in some cases (Figure 14).
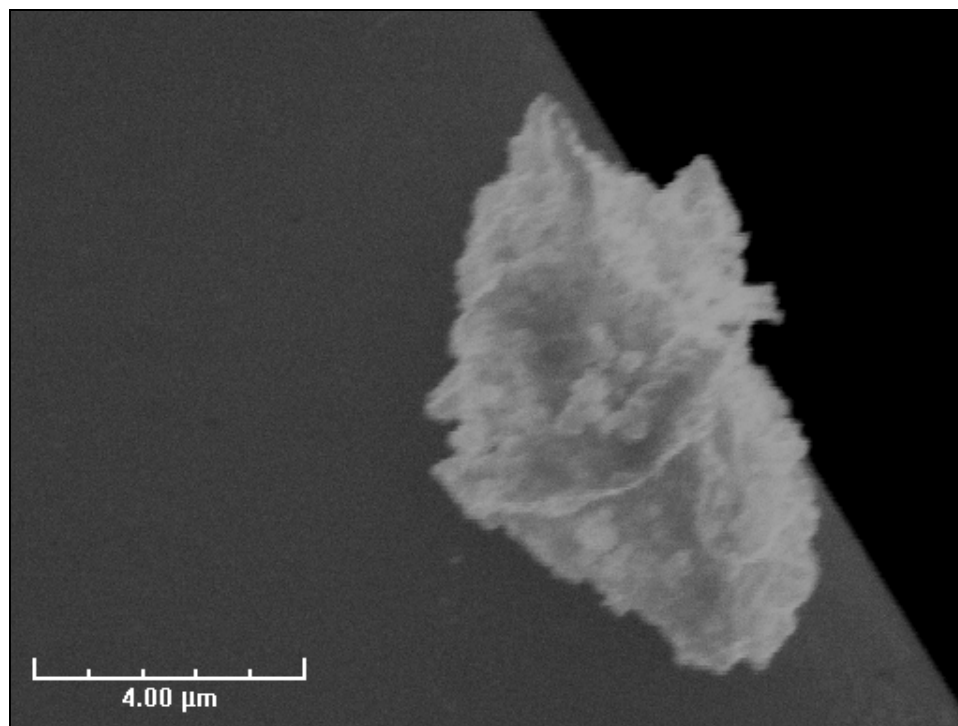
Figure 14 – Scanning electron micrograph of a single, dehydrated *C. parapsilosis* cell bound to a DNPS-type AFM cantilever. Image magnification = 7.0 kX

It should be noted that, while we can see structures that morphologically match our expectations of a *C. parapsilosis* cell, a more rigorous assay should be performed in this verification step. The key issue that must be addressed is that of hydration, *viz.* after cells were attached, it was necessary to hold the cantilevers in a desiccator for several days to drive off moisture to enhance adhesion of the gold coating. This would, presumably, cause a "deflating" of the cell body as the water is removed. More complex chemical treatment of the cantilevers would be necessary to maintain cell morphology after desiccation.

4.4 – Approach Interactions at the Cell-Biomaterial Interface

On examination of the silicone rubber with a cellular modified probe, we see distinct attractive profiles (areas of negative force) present in each approach curve (Figure 15). Interactions begin at 120 nm from the cell surface, and reach a magnitude of approximately 2.5 nN at the cell surface. Both the magnitude and the distance of these interactions are larger than for a bare probe and one modified with HDT.
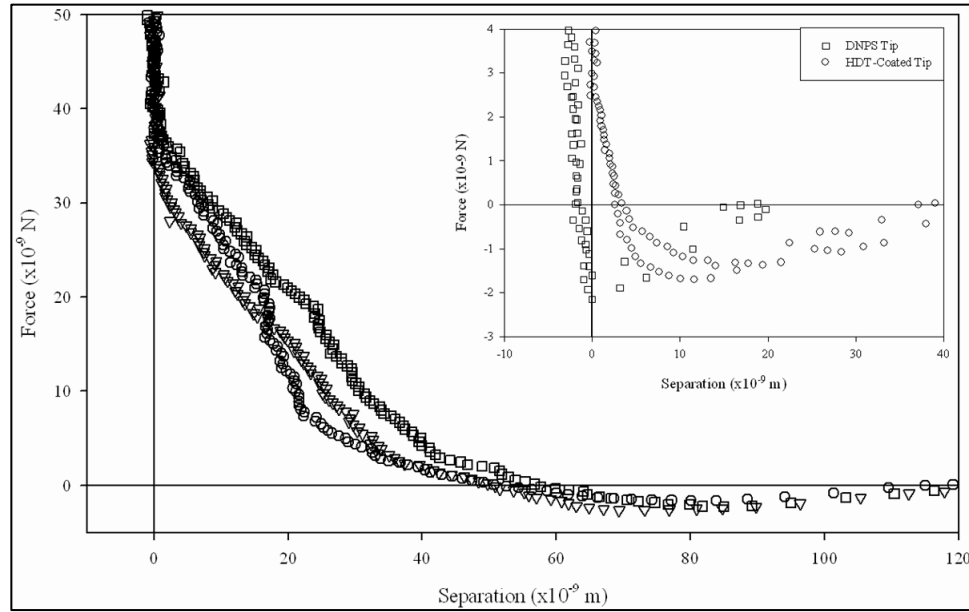
Figure 15 – Approach curves for *C. parapsilosis*-modified cantilever approaching a bare silicone rubber surface. Curves for a bare cantilever and one coated with HDT on the same surface appear at shorter separation distances and weaker attractive forces at the surface in the inset figure.

This range of force interactions may result from heterogeneity in the biomaterial surface, allowing the immobilized cell to interact with discrete areas of the substrate. Surface roughness may be characterized by imaging a representative area of the material using an unmodified cantilever (Figure 16).
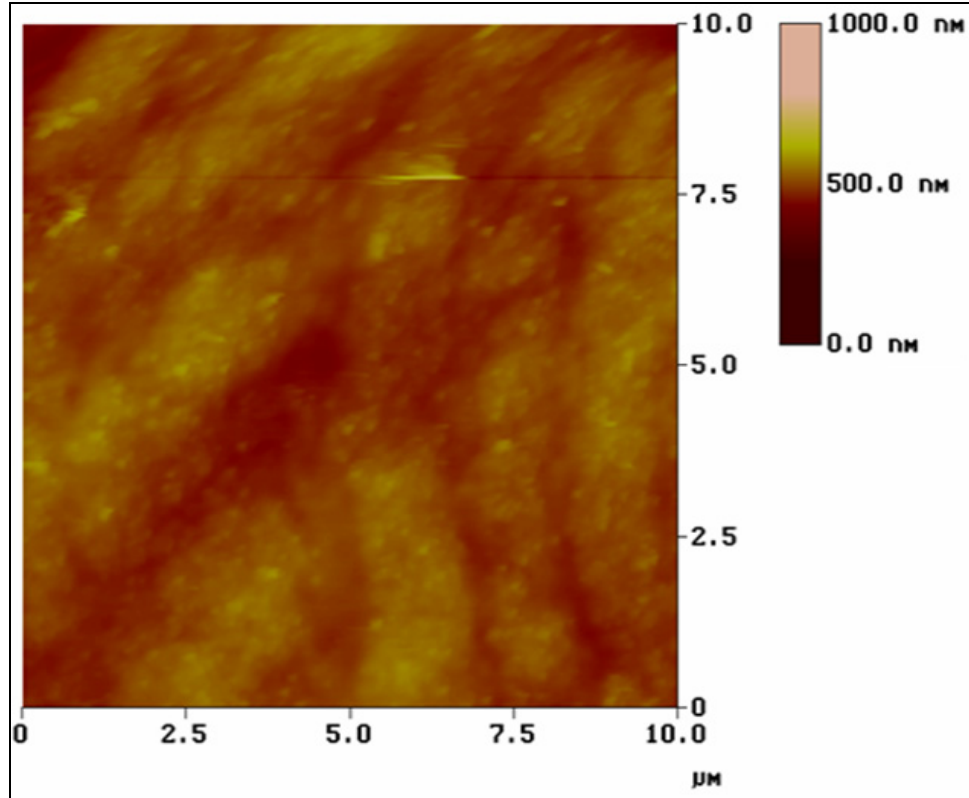
Figure 16 – TappingMode™ AFM image of silicone rubber under 100 mM MES buffer (pH = 7.1). The image shows distinct domains on the surface of the material, offering different areas (possibly with different adhesion affinities) for microbes to adhere. Since the cell is large compared to these domains, it is likely that it will simultaneously interact with a number of these regions.

The image is then processed to obtain the Root Mean Square (RMS) roughness, which is based on Equation (19) [4]. The RMS value obtained from this equation represents the standard deviation of height differences within a given area.

$$RMS = \sqrt{\frac{\sum_{i=1}^{N}\left(Z_i - Z_{Ave}\right)^2}{M}} \tag{19}$$

Where Z_i is the height in a given area, Z_{Ave} is the average height of the entire area, and M is the number of points in that area. We analyzed ten images (i.e., Figure 16) to calculate an average RMS roughness of 40 ± 12 nm (SD) on silicone rubber.

The surface also shows distinct repeating domains, which may influence the interactions of microbial surface structures with the biomaterial, showing different affinities for a "peak" or a "valley". To investigate this qualitatively, we compared the retraction portions of the force cycles (Figure 17) for a bare cantilever on cells bound to glass, and with functionalized probes on bare silicone and a biofilm grown for 3 days on silicone. Data shown represent the different force-distance interactions seen for three substrate/probe combinations.
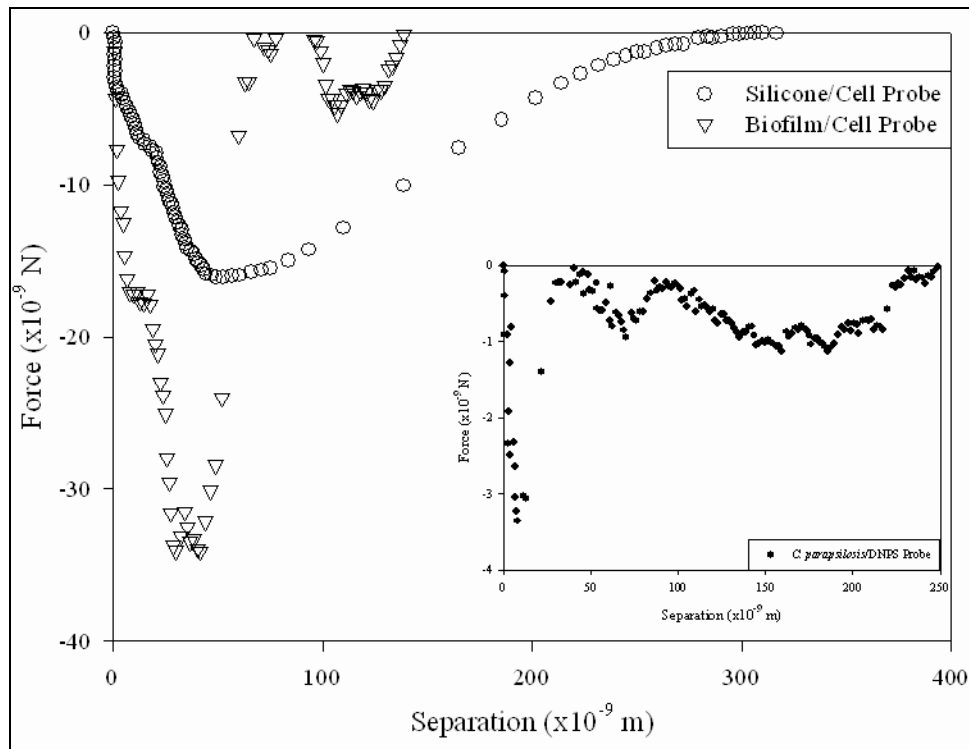
Figure 17 – Retraction curves for *C. parapsilosis*-modified probes on different substrata. One can see that the cells show the highest binding affinity for an established biofilm, with a break off distance of ~40 nm and an adhesive force of ~35 nN. The interaction for silicone rubber and a cell probe indicate a single polymer involved in the interaction. The long range over which the interaction occurs indicates that the polymer is elastic. Interactions between the bare silicon nitride cantilever and *C. parapsilosis* are shown for comparison.

The strongest interactions occur in the biofilm/cell probe system, with an attractive magnitude of ~35 nN at 40 nm from the surface. Further, this system shows

multiple minima in the retraction curve, indicating that multiple polymers take part in the total interaction. For the silicone rubber/cell probe system, we see a single peak with magnitude of ~18 nN, suggesting that only a single polymer plays a significant role in this interaction. The fact that the interaction occurs over such a long range also indicates that the polymer is elastic. Both of these interactions are an order of magnitude stronger than those seen for *C. parapsilosis* probed with a DNPS tip.

4.5 – Approach Interactions at the Cell-Biofilm Interface

AFM approach curves of a modified probe examining a nascent biofilm surface may be seen in Figure 18. Data shown are representative of a biofilm grown for 3 days. Interactions begin at ~250 nm from the biofilm surface, initially showing repulsion. This repulsion reaches a maximum at 2.8 nN, and is immediately followed by an attractive interaction with a maximum of 5 nN. Data were identical for biofilm growth experiments lasting 1 and 3 days in the parallel plate flow chamber, suggesting that, without growth factors, adhesion and detachment of bacteria to the surface reach a steady state relatively quickly.
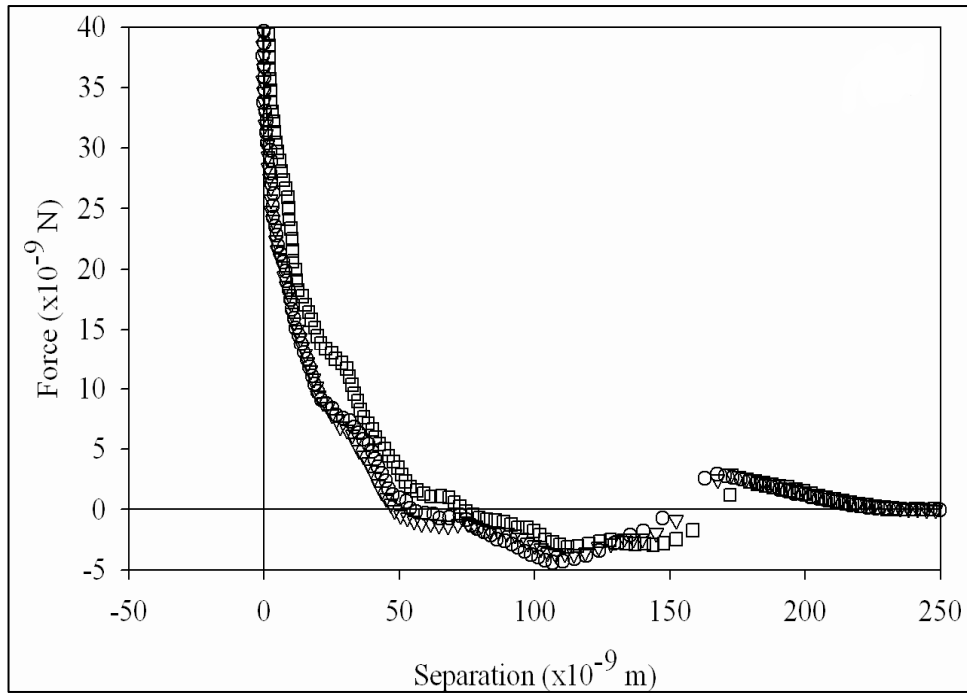
Figure 18 – Approach curves with a cellular modified probe examining a bacterial biofilm grown for 3 days. The majority of the curves show an initial repulsion in the range of 175 – 200 nm, with a characteristic adhesion after this energy barrier has been overcome. The adhesions occur at a shorter range and with larger magnitudes than with a modified probe examining a bare biomaterial surface.

4.6 – Electrophoretic Mobility Analysis

Over the range of ionic strengths, the zeta potential for *P. aeruginosa* increases from -7.96 mV at 20 mM to -3.35 mV at 100 mM (Table 3).

Table 3 – Zeta potential measurements for *C. parapsilosis* and *P. aeruginosa*. All samples were grown at 37°C until $OD_{600} \approx 0.5$ and suspended in MES buffer with varying ionic strength to a cell concentration of ~$1x10^8$ cells/mL.

pH	ζ_{Smol}[a] $(x10^3 \, V)$	μ_E[b] $(x10^8 \, m^2 \cdot [V \cdot s]^{-1})$	Ψ_0[c] $(x10^3 \, V)$
C. parapsilosis			
20 mM	6.81	-5.12	-0.39±0.01	-6.18
40 mM	6.84	-4.54	-0.35±0.18	-3.13
60 mM	6.99	-3.35	-0.26±0.11	-2.09
80 mM	7.01	-6.28	-0.49±0.10	-1.57
100 mM	7.03	-4.74	-0.37±0.10	-1.26
P. aeruginosa			
20 mM	6.95	-7.96	-0.62±0.14	-10.26
40 mM	6.98	-6.67	-0.52±0.07	-5.32
60 mM	6.99	-4.41	-0.34±0.08	-3.57
80 mM	7.01	-5.44	-0.42±0.28	-2.69
100 mM	7.01	-3.35	-0.26±0.10	-2.15

Values of error presented in the above table represent the standard deviation of repeated data sets.

[a] Zeta potential as calculated from the Smoluchowski equation.

[b] Average electrophoretic mobility of microbial culture (N = 4).

[c] Surface potential as calculated from soft-particle DLVO theory; This is equivalent to the zeta potential of the solution.

We see more variation as a function of ionic strength among the data for *C. parapsilosis*, which covers a range of zeta potentials from -6.28 to -3.35 mV. Further, the data do not follow a steady increasing trend, while data for P. aeruginosa do. As

expected, for both microbes, lower values for zeta potentials are calculated using soft-particle theory compared to rigid DLVO with the Smoluchowski equation.   The exception is at low ionic strengths, where soft-particle DLVO theory is least able to represent experimental results.

4.7 – Microbial Interaction Energy Analysis

Using two polar (water and formamide) and one non-polar (diiodomethane) liquids, contact angles on microbial lawns may be translated into surface free energy components. Both microbes are relatively hydrophilic, but *C. parapsilosis* ($\theta_W = 15.17 \pm 11.5^o$ (SD)) is more hydrophilic than *P. aeruginosa* ($\theta_W = 24.42 \pm 1.5^o$ (SD)) (Table 3). These values, and the corresponding surface free energy components, differ significantly from published values for *P. aeruginosa* Olin [39] and *C. parapsilosis* Strain 294 and Strain 289 [36]. Since values for the strains examined in this study were not available, differences in hydrophobicity are expected, owing to differences between the strains.

Simultaneous solution of three instances of the van Oss-Chaudhury-Good equation (8) yields the three surface tension components (Table 4). The values of the apolar surface tension component are then used to calculate the Hamaker constants (Equation (9)), which have values of $6.71 \pm 0.12 \times 10^{-20}$ J (SD) for *C. parapsilosis*, and $5.12 \pm 0.03 \times 10^{-20}$ J (SD) for *P. aeruginosa*. Values for both strains are in good agreement ($< 1 \times 10^{-21}$ J variation) with literature values of similar strains [36, 39].

Table 4 – Microbial contact angle and surface tension data. Microbes were examined under three liquids (Water, Formamide and Diiodomethane). Using the van Oss-Chaudhury-Good equation for the three liquids [101], the three components of surface tension may be calculated.   Hamaker constants (A) follow directly from the values of γ_M^{LW} via Equation (9).

	C. parapsilosis	*P. aeruginosa*
pH	7.03	7.01
θ_W (°)[a]	15.17 ± 11.5	24.42 ± 1.5
θ_F (°)[b]	13.41 ± 1.4	32.28 ± 3.9
θ_D (°)[c]	46.63 ± 1.2	61.69 ± 0.3
γ_M^{LW} (mJ·m^{-2})[d]	36.13 ± 0.65	27.56 ± 0.15
γ_M^{+} (mJ·m^{-2})[e]	1.96 ± 0.39	2.05 ± 0.57
γ_M^{-} (mJ·m^{-2})[f]	51.94 ± 6.42	60.29 ± 3.55
A (x10^{20} J)	6.71 ± 0.12	5.12 ± 0.03

Values of error presented in the above table represent the standard deviation of repeated data sets.

[a] Contact angle of microbial lawn under ddH$_2$O.

[b] Contact angle of microbial lawn under formamide.

[c] Contact angle of microbial lawn under diiodomethane.

[d] Apolar (Lifshitz-van der Waals) parameter of microbial surface free energy.

[e] Electron-accepting parameter of the polar microbial surface free energy.

[f] Electron-donating parameter of the polar microbial surface free energy.

Interaction energy curves for *C. parapsilosis* and *P. aeruginosa* may be seen in Figure 19 and Figure 20, respectively.   Shown are the total, van der Waals and electrostatic interactions, as calculated from soft-particle DLVO and rigid-particle DLVO theories in 100 mM MES buffer.
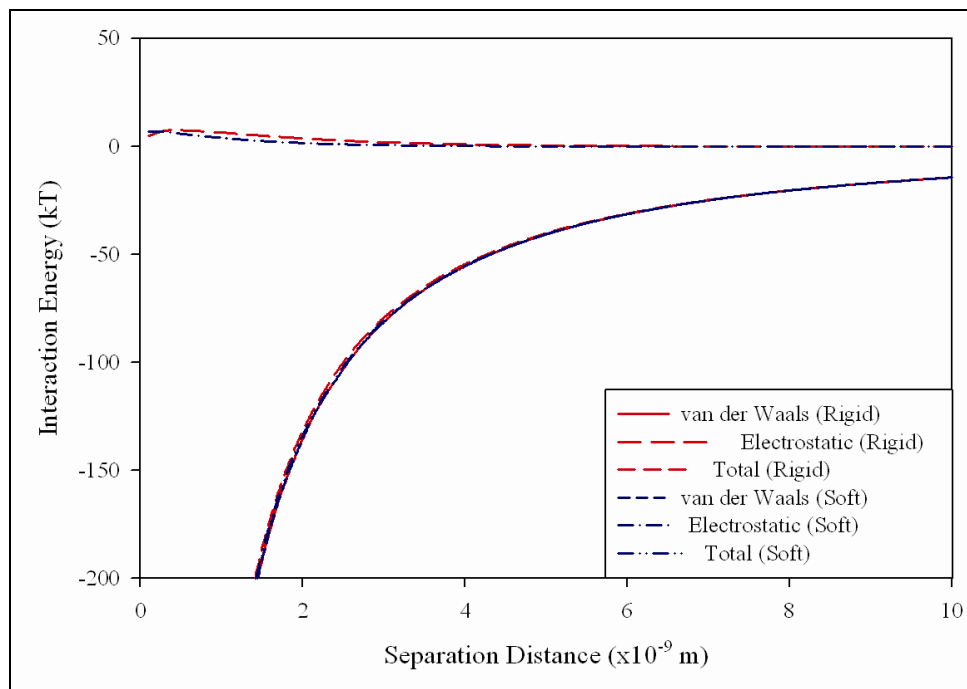
Figure 19 – Interaction energies for *P. aeruginosa* in 100 mM MES buffer. Shown are total energy and the individual contributions for van der Waals and electrostatic interactions, with the differences between soft-particle (points) and rigid-particle (lines) DLVO theories. The two show nearly identical results, save for small differences in electrostatic interactions at very short (<4 nm) separation distances.
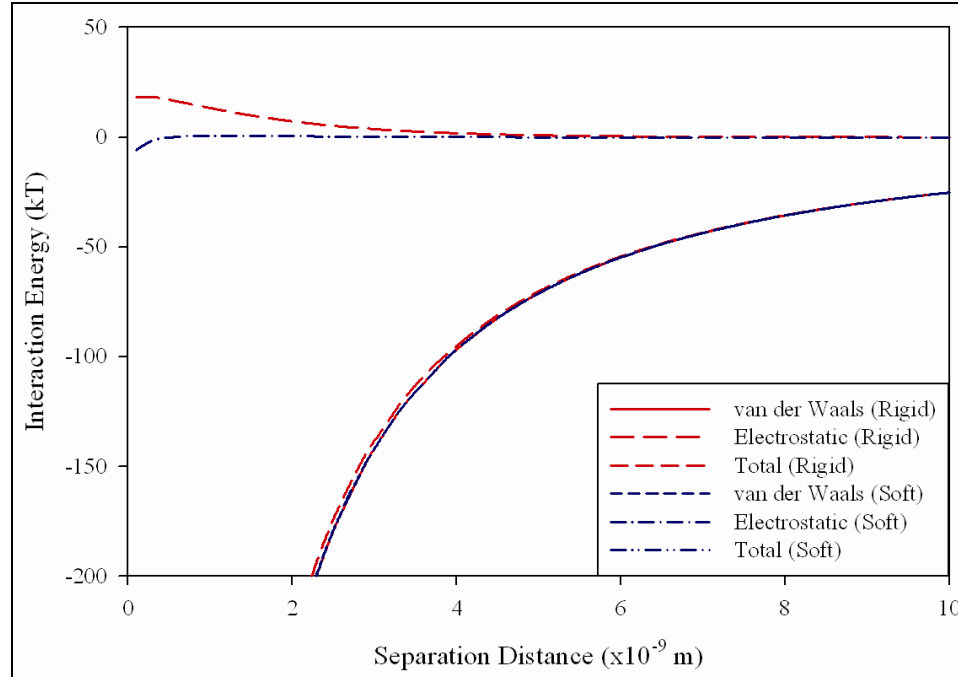
Figure 20 – Interaction energies for *C. parapsilosis* in 100 mM MES buffer. Shown are total energy and the individual contributions for van der Waals and electrostatic interactions, with the differences between soft-particle (points) and rigid-particle (lines) DLVO theories. The two show nearly identical results, save for small differences in electrostatic interactions at very short (<4 nm) separation distances.

For the rigid-particle DLVO calculations, the Smoluchowski equation (6) was used for calculation of microbial surface potentials. *C. parapsilosis* shows no energy barrier preventing adhesion using soft-particle theory, and, in fact, an adhesion of 5.86 k_BT is predicted by the model. An electrostatic repulsion of 18.4 k_BT, starting at 0.3 nm, exists in the calculation based on rigid-particle theory. *P. aeruginosa* shows a 4.83 k_BT electrostatic repulsion at 0.1 nm using rigid-particle DLVO theory, while at the same distance this repulsion has a magnitude of 7.00 k_BT using soft-particle DLVO theory. For both microbes, these small repulsions are greatly outweighed by van der Waals interactions, showing overall negative interaction energy, i.e. attraction, at very small separation distances. Neither classical nor soft-particle DLVO theory agrees with the

behavior seen in AFM force curves (Figure 12 and Figure 13). The models used, however, only account for van der Waals and electrostatic interactions. The fact that there is little difference between the two theories also indicates that the softness of the sample is unimportant in the overall interactions of the microbes. As such, the behavior shown in the force curves must be due to some other physicochemical or physicomechanical phenomena.

4.8 – Modeling Steric Interactions with the Microbial Polymer Brush

The approach curves were fitted using a scaling model for a polymer brush interacting with a flat surface, with the grafted polymer density and equilibrium polymer length as fitting parameters. Graphical fits may be seen in Figure 21 for *C. parapsilosis* and in Figure 23 for *P. aeruginosa*. The steric brush model behaves as a decaying exponential function, and, as such, adhesive behavior (i.e. forces < 0 for the case of *C. parapsilosis*) cannot be predicted by the model. As such, we will fit only the repulsive portion of the data with this model.

63
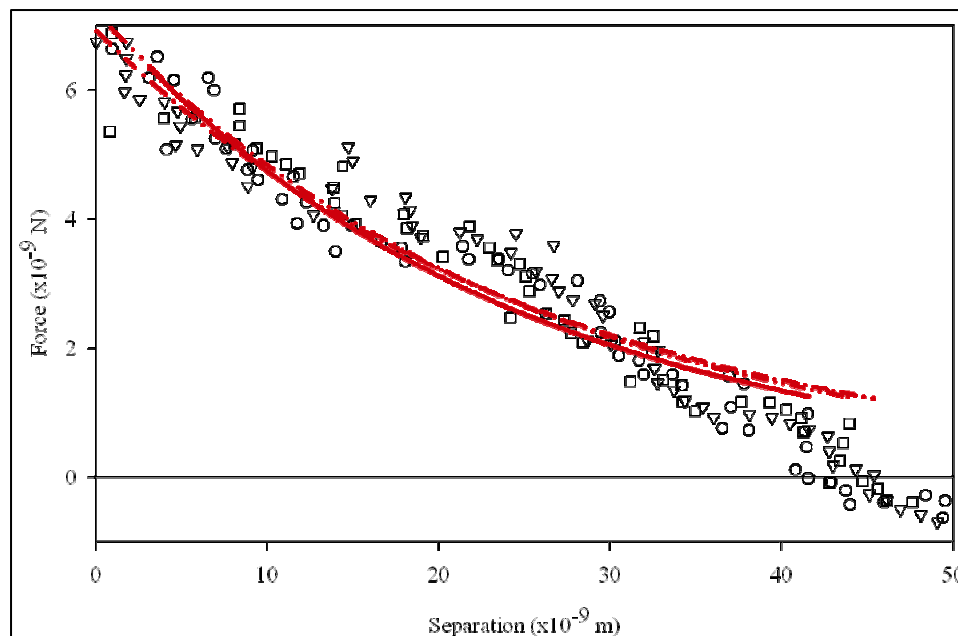
Figure 21 – *C. parapsilosis* **approach curves fitted with the single-brush steric model. Fits are only valid after the attractive interaction occurs, since the steric model cannot account for negative forces.**

C. parapsilosis force-distance interactions demonstrate excellent agreement with the steric model for the repulsive portion of the curve. Values of the fitting parameters for this microbe may be seen in Table 5.

For *P. aeruginosa*, model fits showed excellent mathematical agreement with the collected data. It was evident, however, that the model did not fit the data well at separation distances of ~20 nm from the surface. To verify that the data indeed followed a decaying exponential function, the natural logarithm of the force was plotted against the separation distance (Figure 22).
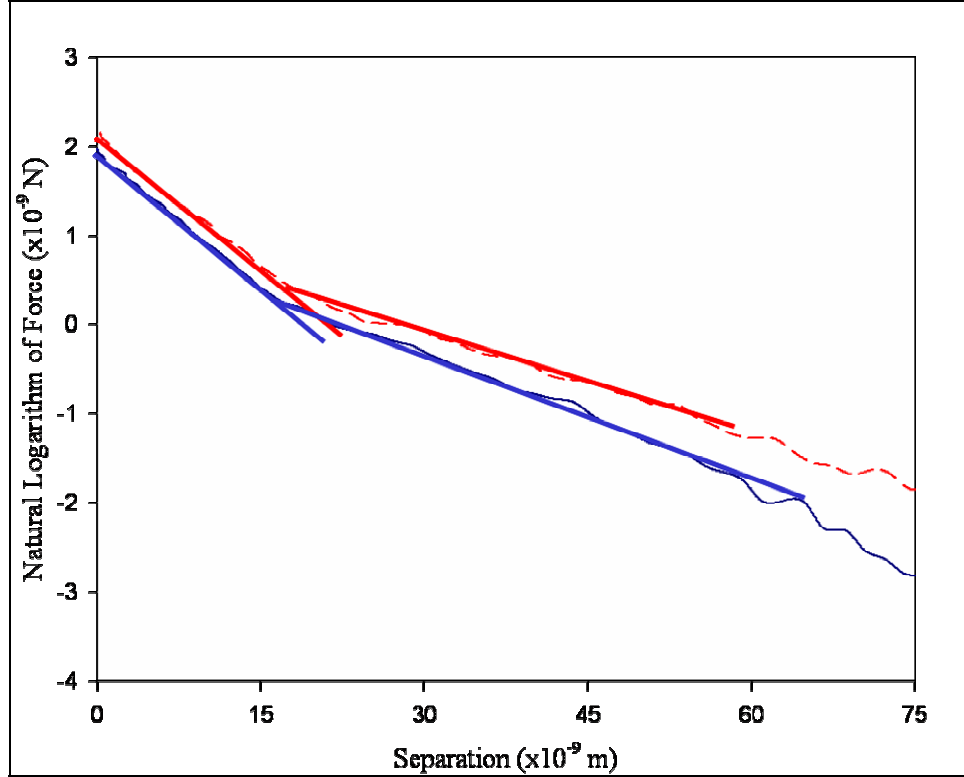
Figure 22 - Plot of LN (Force) versus separation distance. Data show two distinct slopes in the data, indicating the possibility that multiple polymer brushes may be involved in the interaction.

The result of this treatment showed an inflection point in the data set at the distance where the basic steric model fails to fit the data well. As such, we formulated an extension to the steric model which accounts for two polymer layers, each having a different grafting density and equilibrium polymer brush length. Fits with this extended model are shown in Figure 23, and the fitting parameters may be seen in Table 5.

$$F_{St} = 50 k_B T a_p \left[L_1 \Gamma_1^{3/2} e^{-2\pi d/L_1} + L_2 \Gamma_2^{3/2} e^{-2\pi d/L_2} \right] \tag{20}$$
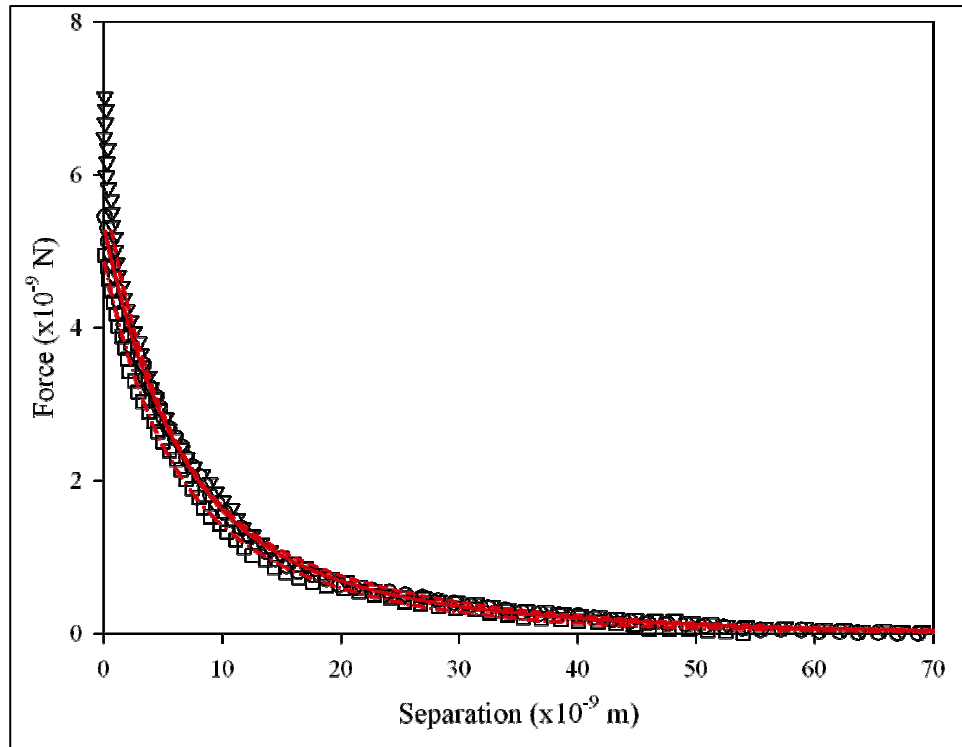
Figure 23 – *P. aeruginosa* approach curves with unmodified silicon nitride probe and fit with the steric model. This model is valid for the entire range of interactions.

For *P. aeruginosa*, fitting with the two-brush model, we see excellent agreement with the data sets ($R^2 > 0.95$). The model produces four values for the fitting parameters (shown in Table 5). Qualitatively, these correspond to the two polymer brushes suggested by the model, with the longer brush having a lower grafting density, and the shorter a higher density. Modeling the cell as a cylinder of radius 1 µm with two hemispherical endcaps, also of radius 1 µm, the grafting density for *P. aeruginosa* is 7.86 x 10^4 polymers·cell^{-1} of the longer polymers, and 3.96 x 10^5 polymers·cell^{-1} of the shorter polymers.

Table 5 – Quantification of equilibrium polymer length and polymer grafting density for *P. aeruginosa* and *C. parapsilosis* as obtained through the steric model.

	C. parapsilosis	*P. aeruginosa*
Γ_1 (x 10^{-16} m^{-2})[a]	3.12	2.48
Γ_2 (x 10^{-16} m^{-2})[a]	-	7.49
L_1 (nm)[b]	160	95
L_2 (nm)[b]	-	24
R^2	0.91	0.99

Five measurements were taken for each cell found and fitted with either the single-brush or double-brush steric model. Data shown represent the average of N = 10 fits. R^2 values are also presented.

[a] Polymer grafting density per unit area.

[b] Equilibrium polymer length of microbial surface features.

4.9 – Modeling Cell Wall Elasticity

An example of the two Hertz indentation models (Equations (15) and (16)) are shown in Figure 24, fitting a *C. parapsilosis* deflection-height curve.
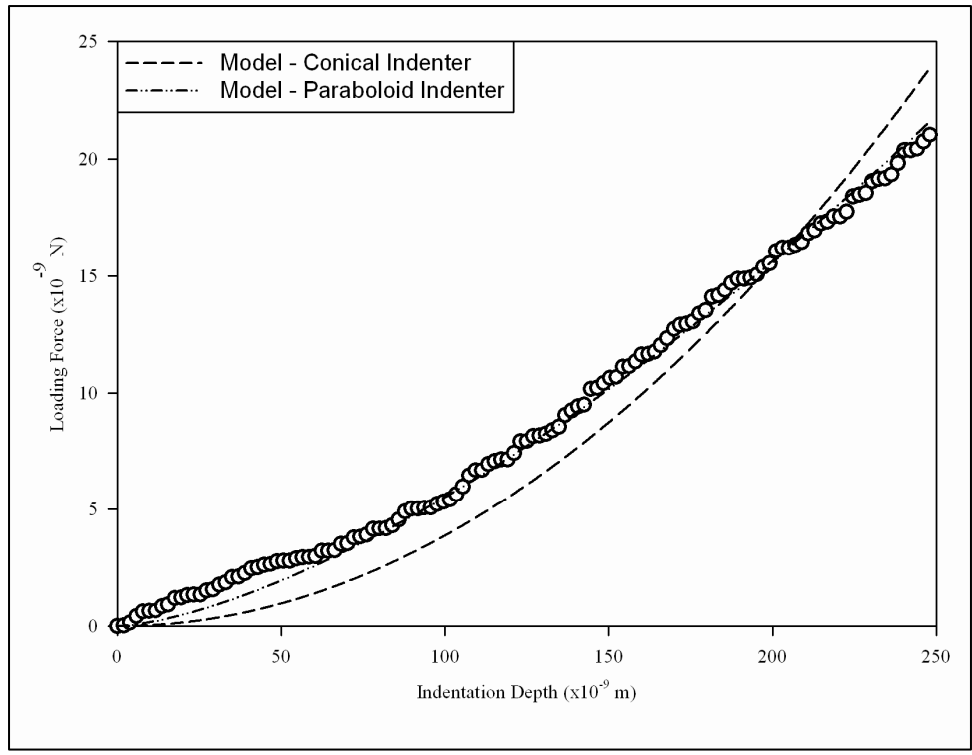
Figure 24 – Example deflection-height curve from a microbial cell. Regression with the Hertz models [Equations (15) and (16)] shows excellent agreement with the data.

Values for the Young's moduli for the five investigated systems may be seen in

Table 6.

Table 6 – Young's modulus values for the five systems examined in this study. The two separate columns take into account the geometry of the probe, according to Equations (15) and (16).

System	Solvent	Young's Modulus (MPa)	
		Conical	Paraboloid
C. parapsilosis, glass	ddH$_2$O	0.773 ± 0.015	0.183 ± 0.004
P. aeruginosa, glass	ddH$_2$O	1.751 ± 0.062	0.338 ± 0.008
Silicone, DNPS tip	100 mM MES	3.013 ± 0.671	0.377 ± 0.035
Silicone, spore probe	100 mM MES	0.208 ± 0.003	0.096 ± 0.001
Biofilm, spore probe	100 mM MES	0.842 ± 0.015	0.259 ± 0.008

Values of error presented in the above table represent the standard deviation of repeated data sets.

As shown in Table 7 the conical model provides the more accurate fits for *P. aeruginosa* data based on the values of the coefficient of determination (R^2). In all other systems (*C. parapsilosis*, Silicone-DNPS Probe, Silicone-Spore Probe, and Biofilm-Spore Probe), however, the paraboloid model better matches the data, in which the loading force is a function of indentation depth raised to the 3/2 power.

Table 7 – Statistical parameters of the fits to the Hertzian models. Note that the highest values of percent variation (Defined as the ratio of the standard deviations of Young's moduli to the Young's moduli themselves) appear in the biofilm system, which is the most heterogeneous surface.

System	Solvent	Conical		Paraboloid	
		R^2	% Variation	R^2	% Variation
C. parapsilosis, glass	ddH$_2$O	0.889	2.67	0.978	2.10
P. aeruginosa, glass	ddH$_2$O	0.901	6.58	0.846	5.46
Silicone, DNPS tip	0.1 M MES	0.779	5.46	0.931	4.11
Silicone, spore probe	0.1 M MES	0.858	2.73	0.969	2.13
Biofilm, spore probe	0.1 M MES	0.943	15.17	0.995	12.17

5 – Discussion

5.1 – Microbial Growth Curves

For valid comparison between experiments, it is vital to harvest and examine cells at the same point in their growth cycle, *viz.* at the same optical density, each time cells are grown. *P. aeruginosa* reaches an acceptable point in its exponential growth phase (O.D.$_{600}$ = 0.50 ± 0.07) in 1.5 – 2.5 hours, while *C. parapsilosis* reaches its ideal growth phase (O.D.$_{600}$ = 0.55 ± 0.06) in 3.5 – 5.0 hours. As can be seen in Figure 10 and Figure 11, the growth behavior of the cells follows an exponential trend. Microbial growth, however, is dependent upon a variety of factors (e.g., temperature, nutrient availability, initial number of cells in culture, the number of viable cells present, etc…), and, as such, small variations between cultures must be expected.

5.2 – Cell Probe Preparation and SEM Analysis

A major goal in formulating this immobilization technique was to minimize the area of the cell that would be chemically treated. An ongoing debate in the scientific community regards whether cells may be exposed to different chemicals before analysis without changing their surface activity. Several groups have shown that treatment in this manner can alter cell wall flexibility, and may also alter the adhesive properties of the cell [17, 51, 52]. Our early work (Figure 25) showed distinct differences in force cycles between microbial cells treated with various fluorescent and visible-spectrum stains and those that were not stained. In this example, cells were treated with different concentrations of the stain Neutral Red, which is described as a "supravital stain" [63], meaning it does not promote apoptosis or lysis when introduced into vital cell cultures. The stain is commonly used in cellular viability and adhesion assays, and is widely considered to be nontoxic for cells [11, 35, 57]. It is clear from our recorded force cycles, however, that the stain alters the properties of the cell surface.
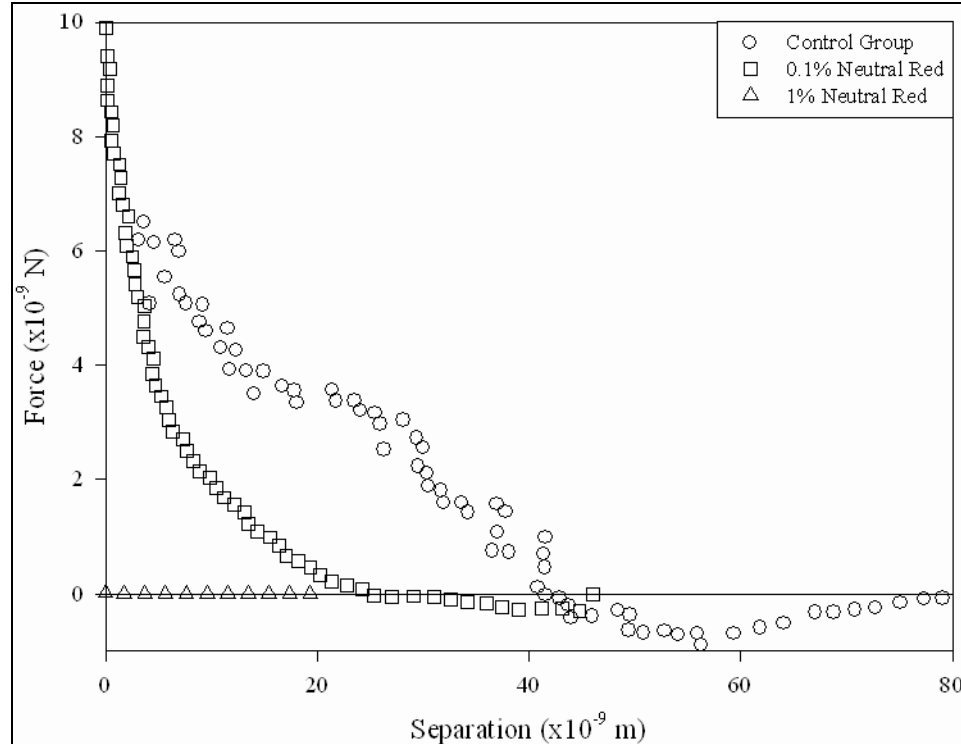
Figure 25 – Illustration of the effects of the chemical stain Neutral Red on AFM force curves. It is clear that the presence of the stain changes the nature of the probe-sample interactions. The decrease in surface repulsion between samples suggests the force is dependent on the concentration of stain present.

While the cell will likely survive treatment with Neutral Red, its surface properties are altered. As such, we believe that minimizing chemical treatment of the cell surface with any agent will give results most closely approximating those found *in vivo*. Further investigation of the physicochemical properties of microbial cell walls and their structures and their relationship to chemical treatment may prove to be exceptionally interesting.

Examination of the cellular probes with SEM showed cells bound to the cantilever with multiple cells present in some cases. Since the height of the tips is small (~1 μm) relative to the height of the cells, the chemisorbed Candida would be the major bodies

interacting with the sample surfaces. It was also noted that, while the cells were not perfectly aligned at the apex of each cantilever, the tips themselves were, in all cases, off-center as well. Any changes in force curves due to this misalignment of the tip are corrected for during the calibration procedure. The same technique should be directly applicable to correcting for an off-center cell chemisorbed to the cantilever.

5.3 – Approach Interactions at the Cell-Biomaterial Interface

For a modified probe interacting with a biomaterial, adhesive interactions exist within the range of equilibrium polymer lengths for *C. parapsilosis*. The domains evident on the polymer suggest that the heterogeneity of the surface could lead to a variety of interactions, depending on whether the cell surface structures interacted with a "peak" or a "valley." Therefore, it is possible that long, proteinaceous surface structures (i.e., flagella, fimbriae), if present, may interact with these domains before the majority of the polymers on the cell surface. The role of such structures in lectin-ligand binding to specific sites has been investigated by a number of groups [88, 89, 95]. These groups have demonstrated that cell surface structures are critical in certain lock-and-key mechanisms, and that the lectins interact with specific saccharide residues. Singh et al. [89] discussed the existence of cell-cell interactions in terms of specific biological systems, including bacteria, plants and yeasts. While no evidence has been found in the open literature examining such structures on *C. parapsilosis*, various other yeasts (*Kluyveromyces bulgaricus, Saccharomyces cerevisiae, S. ludwigii and Brandeiraea simplicifolia*) were shown to produce them.

Structures protruding from the cell surface would also be able to specifically interact with either high or low points on the surface, since these structures are very narrow as compared to the domains on the materials. However, the cell itself is large as compared to these domains, and the majority of the adhesions occur within the range of equilibrium polymer lengths for the cell. Affinities, as shown in the retraction curves in Figure 17, demonstrate unique values for each substrate. The strongest interactions occur with bare silicone, with only one peak in the retraction curve. This indicates that only one type of polymer is interacting with the probe, as compared to the multiple peaks for functionalized probes on a biofilm substrate. So, while long cell surface structures may interact with different portions of the biomaterial surface, the similarity of interactions over several areas leads us to believe that a bulk or average area of contact will play the dominant role in cellular adhesion.

It is therefore within reason to say that the polymer brush, which is distributed across the cell surface and has a thickness that may be mathematically quantified, is the main feature of the cell interacting with the biomaterial. Further, since a distinct inflection occurs where adhesion ends and repulsion begins, we may conclude that the point of maximum adhesion (most negative force) is the maximum compression force of the polymers on the cell surface. After this point, the brush cannot be compacted further, and begins pushing back against the probe loading force as the probe comes into contact with the material surface.

5.4 – Approach Interactions at the Cell-Biofilm Interface

Interactions between a modified probe and a nascent biofilm also exhibit a characteristic attraction on approach. However, immediately before this adhesion occurs, a long-range (250 nm) repulsion takes place. This can be attributed to a combination of electrostatic double layer effects associated with the polymer brushes on each microbe, as well as steric effects.

As the "planktonic" *C. parapsilosis* moves closer to the surface, the strong adhesive interaction begins to dominate. This suggests that an initial energy barrier must be overcome to reach an energetic minimum favoring sessile behavior. Therefore, the planktonic microbe must have sufficient force, associated with bulk flow, gravitational settling or the cell's inherent mobility, to initially bind to a biofilm.

Adhesive peaks correlate to the equilibrium polymer lengths of *P. aeruginosa*, occurring at shorter distances than those seen for a modified probe and a bare biomaterial surface. The adhesions are also of much higher (as much as 3x greater) magnitude than those seen for a modified probe-bare biomaterial system. This behavior suggests that planktonic cells have a higher affinity for binding to surfaces on which a biofilm is already growing, and that the cells, once bound, will have a greater probability of remaining bound, since a perturbation of greater magnitude will be required to dislodge the cell.

Microbial adhesion to medical implant materials and biofilms growing on those materials is a complex topic, but one that is essential to the prevention and elimination of implant-associated infections. Using AFM and supporting technologies, it is possible to characterize how strongly a microbial cell interacts with a bare or biofilm-coated

biomaterial surface. Application of mathematical models allows for quantification of interaction energies that are useful in constructing new theories and in designing materials that protect the host from microbial colonization.

5.5 – Microbial Interaction Energy Analyses

Microbial surface potentials were calculated using classical DLVO theory and the soft-particle DLVO equations. DLVO calculations based on assuming the zeta potential equal to the surface potential (i.e. classical DLVO calculations) predicted higher values for surface potential compared to potentials calculated from the soft-particle equations. Departure from the experimental measurements was most significant in solutions with low salt concentrations.

For *C. parapsilosis* (Figure 20), there was poor agreement with soft-particle DLVO theory, in terms of calculating the surface potential for the cell. Plotting calculated versus experimental electrophoretic mobilities (data not shown), followed by a linear regression of these data, gave a value of $R^2 = 0.219$ and a spatial charge density (*ZN*) of -0.0196 mol·L^{-1}. Fungal cell walls often contain cellulose, chitin, or both [67], which greatly increases cell wall rigidity. So, while various bacterial strains, such as *E. coli* [7], *P. putida*, *P. aeruginosa* [45], and *S. salivarius* [12], show better agreement with soft-particle DLVO theory, *C. parapsilosis* would presumably interact as a more rigid particle. Soft-particle DLVO theory provides no appreciable benefit over classical theory in this case.

Since *P. aeruginosa* (Figure 19) does not contain these rigid materials, we expected to see a better agreement with soft-particle DLVO theory. This was true, with

soft-particle theory providing a fit with $R^2 = 0.671$ and $ZN = -0.0336$ mol·L^{-1}. The model fit is not as accurate as has been observed for other bacteria [7], perhaps because more data, especially at low ionic strengths, is necessary to completely characterize the system.

On the whole, neither classical nor soft-particle DLVO theory quantitatively predicts the interactions seen for either *P. aeruginosa* or *C. parapsilosis*. This may be due to the fact that only three types of interactions (electrostatic, van der Waals, and softness effects) were accounted for in the model. It may be beneficial in the future to include other interactions in the mathematical model to obtain a clearer picture of the forces involved in the behavior of these two microbes.

Further investigation of DLVO-type interactions may have included the use of extended DLVO theory (XDLVO) [101, 112, 113], which describes acid-base interactions. However, recent work in our group has shown that XDLVO produces unrealistically high energy barriers at low separation distances for *P. putida* KT2442 [6]. While acid-base interactions may exist in the forms of charged species on the microbial surface, these previous results prompted us to neglect their effect in the overall interaction energy profiles.

5.6 – Modeling Steric Interactions with the Microbial Polymer Brush

For *C. parapsilosis*, we see excellent agreement between the repulsive data points and the steric model. This demonstrates that, after the interactions causing attraction take place (Figure 13), steric interactions due to the microbial polymer brush become dominant. Where this model is incapable of fitting attractive interactions and the classical and soft DLVO theories did not predict an attractive minimum in the energy

profiles, the source of the attractive interaction seen for *C. parapsilosis* has still not been identified.

The two-brush steric model fits the repulsive regions of the approach curves for *P. aeruginosa* very well, indicating that steric forces play a significant role as the probe approaches the cells (Figure 23). Physically, this model represents the interactions of an elastic polymer brush with a surface (in this case, the AFM probe), where the force increases as the brush is further compressed. So, the increasing repulsive force seen as the probe approaches the cell is indicative of cell surface structures pushing back against the cantilever due to their own inherent elasticity and increasing rigidity.

There were no attractive interactions seen for *P. aeruginosa*. Qualitatively similar results have been observed from AFM measurements on *E. coli* JM109 [7], *Burkholderia cepacia* G4, and *P. putida* KT2442 [21]. The hydrophobicity and surface potentials of *P. putida* and *P. aeruginosa* are similar, and it is not surprising that strong repulsive interactions are observed between the polymer brush and the AFM probe for both bacterial strains.

5.7 – Modeling Cell Wall Elasticity

The model fits from the two Hertzian indentation models match the experimental data very well, with R^2 values above 0.9 for most cases. The validity of the individual equations depends on whether the deflection-height curves follow a quasi-quadratic (δ^2) or a fractional ($\delta^{3/2}$) trend. In the case of the *P. aeruginosa* data, a quasi-quadratic relationship is seen, and so the conical model is the most applicable geometry for this system. In the other four systems examined, however, a fractional dependency of force

on indentation depth is seen, meaning that these conformations are better matched by paraboloid geometry.

Contrary to our expectation, values of the Young's modulus were lower for *C. parapsilosis* than for *P. aeruginosa*, indicating that *P. aeruginosa* has a less elastic cell wall than *C. parapsilosis*. This is not reasonable, given that the cell wall of a fungus should be more rigid than that of a bacterium. Other groups applying these models have seen that the conical models provide the best fits in all cases. Touhami et al [96] showed that the Young's modulus for the surface of *S. cerevisiae* is 0.6 ± 0.4 MPa, which is significantly higher than our calculated moduli for *C. parapsilosis*, and that our previous assumption of the presence of a rigid material in the cell wall may be valid. However, a better comparison would be to obtain the Young's modulus for another Candida strain. These values were unavailable after a search of the open literature. Further, the paraboloid model provided the best fit to our data, while data for *S. cerevisiae* was best approximated by the conical model.

Using the same models, Abu-Lail reported a Young's modulus of 0.6 ± 0.4 MPa for the cell envelope of *E. coli* JM109 [5]. This value is also higher than for *P. aeruginosa*, indicating that *E. coli* is a more rigid cell. Again, comparing values of Young's modulus to another Pseudomonad would estimate the validity of the model more empirically.

It is important to note that the Hertzian models are valid only in the cases where significant adhesions between the probe and sample do not exist [96]. In these cases, the Johnson-Kendall-Roberts (JKR) theory [55] is most applicable. Since adhesions of varying magnitudes exist in the *C. parapsilosis*, Silicone-DNPS probe, Silicone-Spore

probe and Biofilm-Spore probe systems, it would be of interest to compare the results obtained by Hertzian modeling to those obtained from JKR theory. Further, other mathematical formulations describing the contact to two particles in solution (e.g., Bradley rigid, Derjaguin-Muller-Toporov, Maugis-Dugdale) may be equally valid, depending on the elasticity of the particles and the total thermodynamic work performed in deforming the particles [54]. Using these two parameters, it is possible to characterize the system with the most appropriate model. Enumerating these parameters in the context of the above systems would allow for characterization in terms of the most physically relevant models.

6 – Conclusions

We examined two medically-important microbes in order to characterize their affinity for biomaterial and biofilm surfaces. Steric interactions play significant roles in the approach of silicon nitride probes to both *C. parapsilosis* and *P. aeruginosa*. These interactions do not, however, explain the adhesive interactions seen for *C. parapsilosis*. Further, the adhesions are not mathematically predicted in soft-particle or rigid-particle DLVO interaction energy analysis. As such, other forces must be responsible for the adhesions present in the force cycles.

Planktonic microbes show adhesive interactions with bare and biofilm-coated biomaterial surfaces, with a clear point of maximum adhesive strength visible in the approach portions of the force cycles. These occur at approximately the same distance for both, with biofilm-coated surfaces causing a stronger adhesive interaction. In biofilm

systems, however, there is an initial repulsion that must be overcome before an adhesion may take place.

We have also demonstrated that established methods of force curve analysis show inconsistencies when involving a polymer brush on the sample, the probe, or both. Additional experimentation is necessary to accurately quantify the role of the polymer brush in AFM approach curves involving attraction, but application of the constant compliance region as the reference point in defining zero separation should be an adequate approximation of the sample surface.

The procedure to examine this model system allows us to characterize cell-biomaterial and cell-cell interactions at the scales of force and distance at which they occur. We are refining our immobilization technique so that single cells can be attached to form the probe. Further examination of different systems of microbes and materials will provide quantitative data for the design of new materials that are less susceptible to microbial attack, and will save many dollars and many lives in the process.

References

1. *The Development of AFM*. http://www.pacificnanotech.com/tech/history.htm, (Accessed 24 September, 2003).

2. *Nano Personalities - Dr. Christoph Gerber*. http://www.nano.org.uk/personalities5.htm, (Accessed 24 September, 2003).

3. *Dimension 3100 Manual Ver. 4.43B*; Digital Instruments, Veeco Metrology Group: 1997; Section 6.3.1.

4. *Scanning Probe Microscopy Training Notebook*; Digital Instruments, Veeco Metrology Group: 1998; 39-40.

5. Abu-Lail, N I. "The Effect of Biopolymer Properties on Bacterial Adhesion: An Atomic Force Microscopy (AFM) Study". *Ph.D. Dissertation*, Worcester Polytechnic Institute, Worcester, Massachusetts, 2003.

6. Abu-Lail, N I and T A Camesano. *"Role of ionic strength on the relationship of biopolymer conformation, DLVO contributions and steric interactions to bioadhesion of Pseudomonas putida KT2442,"* Biomacromolecules, 2003. **4**: p. 1000.

7.   Abu-Lail, N I and T A Camesano. *"Role of lipopolysaccharides in the adhesion, retention and transport of Escherichia coli JM109,"* Env. Sci. Technol., 2003. **37**: p. 2173.

8.   Alexander, S. *"Adsorption of chain molecules with a polar head: A scaling description,"* J. Phys. (Paris), 1977. **38**(8): p. 983.

9.   Bassler, B L. *"How bacteria talk to each other: regulation of gene expression by quorum sensing,"* Curr. Opin. Microbiol., 1999. **2**(6): p. 582.

10.   Binnig, G, C F Quate, and C Gerber. *"Atomic force microscope,"* Phys. Rev. Lett., 1986. **56**(9): p. 930.

11.   Borenfreund, E and J A Puerner. *"A simple quantitative procedure using monolayer cultures for cytotoxicity assay (HTD/NR-90),"* J. Tiss. Cult. Meth., 1984. **9**: p. 7.

12.   Bos, R, H C van der Mei, and H J Busscher. *"'Soft-particle' analysis of the electrophoretic mobility of a fibrillated and non-fibrillated oral streptococcal strain: Streptococcus salivarius,"* Biophys. Chem., 1998. **74**: p. 251.

13.   Bos, R, H C van der Mei, and H J Busscher. *"Physico-chemistry of initial microbial adhesive interactions - its mechanisms and methods for study,"* FEMS Microbiol. Rev., 1999. **23**: p. 179.

14.   Boström, M, D R M Williams, and B W Ninham. *"Specific ion effects: Why DLVO theory fails for biology and colloid systems,"* Phys. Rev. Lett., 2001. **87**(16): p. 1681031.

15.   Bowen, W R, et al. *"Direct measurement of the force of adhesion of a single biological cell using an atomic force microscope,"* Coll. Surf. A, 1998. **136**: p. 231.

16.   Bowen, W R, R W Lovitt, and C J Wright. *"Direct quantification of Aspergillus niger spore adhesion in liquid using an atomic force microscope,"* J. Coll. Int. Sci., 2000. **228**: p. 428.

17.   Burks, G A, et al. *"Macroscopic and nanoscale measurements of the adhesion of bacteria with varying outer layer surface composition,"* Langmuir, 2003. **19**(6): p. 2366.

18. Burnham, N A and A J Kulik, *Surface Forces and Adhesion*, in *Handbook of Micro/Nano Tribology*, B. Bhushan, Editor. 1999, CRC Press: Boca Raton. p. 247-271.

19. Butt, H-J, et al. *"Steric forces measured with the atomic force microscope at various temperatures,"* Langmuir, 1999. **15**: p. 2559.

20. Caccavo, F J and A Das. *"Adhesion of dissimilatory Fe(III)-reducing bacteria to Fe(III) minerals,"* Geomicrob. J., 2002. **19**(2): p. 161.

21. Camesano, T A and B E Logan. *"Probing bacterial electrosteric interactions using atomic force microscopy,"* Env. Sci. Technol., 2000. **34**: p. 3354.

22. Camesano, T A, M J Natan, and B E Logan. *"Observation of changes in bacterial cell morphology using tapping mode atomic force microscopy,"* Langmuir, 2000. **16**: p. 4563.

23. Casimir, H B G and D Polder. *"The Influence of Retardation on the London-van der Waals Forces,"* Phys. Rev., 1948. **73**: p. 360.

24.   Centeno, A, et al. *"Modulation of Candida albicans attachment to human epithelial cells by bacteria and carbohydrates,"* Infect. Immun., 1983. **39**(3): p. 1354.

25.   Costerton, J W. *"Overview of microbial biofilms,"* J. Ind. Microbiol., 1995. **15**: p. 137.

26.   Costerton, J W, G G Geesey, and K-J Cheng. *"How bacteria stick,"* Sci. Am., 1978. **238**: p. 86.

27.   Costerton, J W, et al. *"Microbial biofilms,"* Annu. Rev. Microbiol., 1995. **49**: p. 711.

28.   de Gennes, P G. *"Polymers at an interface: A simplified view,"* Adv. Coll. Int. Sci., 1987. **27**: p. 189.

29.   Derjaguin, B V and L Landau. *"Theory of the stability of strongly charged lyophobic sols and the adhesion of strongly charged particles in solutions of electrolytes,"* Acta Physicochim. (URSS), 1941. **14**: p. 633.

30.   Donlan, R M. *"Biofilms: Microbial life on surfaces,"* Emerg. Infect. Dis., 2002. **8**(9): p. 881.

31.   Ducker, W A and T J Senden. *"Measurement of forces in liquids using a force microscope,"* Langmuir, 1992. **8**: p. 1831.

32.   Dufrêne, Y F. *"Application of atomic force microscopy to microbial surfaces: from reconstituted cell surface layers to living cells,"* Micron, 2001. **32**: p. 153.

33.   Dufrêne, Y F, et al. *"Probing molecular interactions and mechanical properties of microbial cell surfaces by atomic force microscopy,"* Ultramicroscopy, 2001. **86**: p. 113.

34.   Egorenkova, I V, et al. *"Role of the polysaccharide components of Azospirillum brasilense capsules in bacterial adsorption on wheat seedling roots,"* Microbiology (Moscow, Russian Federation), 2001. **70**(1): p. 36.

35.   Flick, D A and G E Gifford. *"Comparison of in vitro cell cytotoxic assays for tumor necrosis factor,"* J. Immunol. Meth., 1984. **68**: p. 167.

36.   Gallardo-Moreno, A M, et al. *"Analysis of the hydrophobic behaviour of different strains of Candida parapsilosis under two growth temperatures,"* Coll. Surf. B: Biointerfaces, 2003. **28**: p. 119.

37.   Gottenbos, B, H C van der Mei, and H J Busscher. *"Initial adhesion and surface growth of Pseudomonas aeruginosa on negatively and positively charged poly(methacrylates),"* J. Mater. Sci. Mater. Med., 1999. **10**: p. 853.

38.   Gottenbos, B, H C van der Mei, and H J Busscher. *"Initial adhesion and surface growth of Staphylococcus epidermidis and Pseudomonas aeruginosa on biomedical polymers,"* J. Biomed. Mater. Res., 2000. **50**: p. 208.

39.   Grasso, D, et al. *"Impact of physiological state on surface thermodynamics and adhesion of Pseudomonas aeruginosa,"* Env. Sci. Technol., 1996. **30**: p. 3604.

40.   Gregory, J. *"Approximate expressions for retarded van der Waals interaction,"* J. Coll. Int. Sci., 1981. **83**(1): p. 138.

41.   Gristina, A G. *"Biomaterial-centered infection: Microbial adhesion versus tissue integration,"* Science, 1987. **237**: p. 1588.

42.   Gunning, P A, et al. *"Comparative imaging of Pseudomonas putida bacterial biofilms by scanning electron microscopy and both DC contact and AC non-contact atomic force microscopy,"* J. Appl. Bacteriol., 1996. **81**: p. 276.

43.   Hamaker, H C. *"London-van der Waals attraction between spherical particles,"*

Physica (Amsterdam), 1937. **4**: p. 1058.

44.   Hansma, H G, et al. *"Properties of biomolecules measured from atomic force*

microscopy images: A review," J. Struct. Biol., 1997. **119**: p. 99.

45.   Hayashi, H, et al. *"Soft particle analysis of bacterial cells and its interpretation of*

cell adhesion behaviors in terms of DLVO theory," Coll. Surf. B: Biointerfaces,

2001. **22**: p. 149.

46.   Heard, S O. *"Catheter-related infection: Diagnosis, prevention and treatment,"*

Ann. Acad. Med. Singapore, 2001. **30**: p. 419.

47.   Heinz, W F and J H Hoh. *"Spatially resolved force spectroscopy of biological*

surfaces using the atomic force microscope," Nanotechnology, 1999. **17**: p. 143.

48.   Helmus, M N, *Biomaterials in the Design and Reliability of Medical Devices*.

Tiss. Eng. Int. 2002, Georgetown, TX: Eurekah.com/Landes Bioscience.

49.   Hertz, H. *"Über die Berührung fester elastischer Körper,"* J. Reine Agnew.

Math., 1882. **92**: p. 156.

50. Hogg, R, T W Healy, and D W Fuerstenau. *"Mutual coagulation of colloidal dispersions,"* Trans. Faraday Soc., 1966. **62**: p. 1638.

51. Hoh, J H and C A Schoenenberger. *"Surface morphology and mechanical properties of MDCK monolayers by atomic force microscopy,"* J. Cell Sci., 1994. **107**: p. 1105.

52. Hopwood, D. *"Theoretical and practical aspects of glutaraldehyde fixation,"* Histochem. J., 1972. **4**(4): p. 267.

53. Hyonchol, K, et al. *"Quantification of fibronectin and cell surface interactions by AFM,"* Coll. Surf. B: Biointerfaces, 2002. **25**: p. 33.

54. Johnson, K L and J A Greenwood. *"An adhesion map for the contact of elastic spheres,"* J. Coll. Int. Sci., 1997. **192**: p. 326.

55. Johnson, K L, K Kendall, and A D Roberts. *"Surface energy and the contact of elastic solids,"* Proc. R. Soc. Lond. A., 1971. **324**: p. 301.

56. Khardori, N and M Yassien. *"Biofilms in device-related infection,"* J. Ind. Microbiol., 1995. **15**: p. 141.

57.   Kull, F C and P Cuatrecasas. *"Preliminary characterization of the tumor cell cytotoxin in tumor necrosis serum,"* J. Immunol., 1981. **126**: p. 1279.

58.   Lee, G U, L A Chrisey, and R J Colton. *"Direct measurement of the forces between complementary strands of DNA,"* Science, 1994. **266**(5186): p. 771.

59.   Levin, A S, et al. *"Candida parapsilosis fungemia associated with implantable and semi-implantable central venous catheters and the hands of healthcare workers,"* Diagn. Microbiol. Infect. Dis., 1998. **30**: p. 243.

60.   Losic, D, J G Shapter, and J J Gooding. *"Concentration dependence in microcontact printing of self-assembled monolayers (SAMs) of alkanethiols,"* Electrochem. Comm., 2001. **3**: p. 722.

61.   Lower, S K, C J Tadanier, and M F Hochella Jr.. *"Measuring interfacial and adhesion forces between bacteria and mineral surfaces with biological force microscopy,"* Geochim. Cosmochim. Acta, 2000. **64**(18): p. 3133.

62.   Lower, S K, C J Tadanier, and M F Hochella Jr.. *"Dynamics of the mineral-microbe interface: Use of biological force microscopy in biogeochemistry and geomicrobiology,"* Geomicrob. J., 2001. **18**: p. 63.

63.   Lowik, C W, et al. *"Quantification of adherent and nonadherent cells cultured in 96-well plates using the supravital stain neutral red,"* Analytical Biochemistry, 1993. **213**: p. 426.

64.   Lupetti, A, et al. *"Horizontal transmission of Candida parapsilosis candidemia in a neonatal intensive care unit,"* J. Clin. Microbiol., 2002. **40**(7): p. 2363.

65.   Lyczak, J B, C L Cannon, and G B Pier. *"Establishment of Pseudomonas aeruginosa infection: lessons from a versatile opportunist,"* Microb. Infect., 2000. **2**: p. 1051.

66.   Ma, Q, et al. *"Protein secretion systems of Pseudomonas aeruginosa and P. fluorescens,"* Biochim. Biophys. Acta, 2003. **1611**: p. 223.

67.   Madigan, M T, J M Martinko, and J Parker, *Biology of Microorganisms*. 9 ed. 2000, Upper Saddle River, NJ: Prentice Hall. 730.

68.   Mermel, L A, et al. *"Guidelines for the management of intravascular catheter-related infections,"* Clin. Infect. Dis., 2001. **32**(9): p. 1249.

69. Michiels, K W, C L Croes, and J Vanderleyden. *"Two different modes of attachment of Azospirillum brasilense Sp7 to wheat roots,"* J. Gen. Microbiol., 1991. **137**(9): p. 2241.

70. Mrksich, M, et al. *"Controlling cell attachment on contoured surfaces with self-assembled monolayers of alkanethiols on gold,"* Proc. Natl. Acad. Sci. USA, 1996. **93**(20): p. 10775.

71. Munakata-Marr, J, et al. *"Enhancement of trichloroethylene degradation in aquifer microcosms bioaugmented with wild type and genetically altered Burkholderia (Pseudomonas) cepacia G4 and PR1,"* Env. Sci. Technol., 1996. **30**: p. 2045.

72. Nguyen, M H, et al. *"The changing face of candidemia: Emergence of non-Candida albicans species and antifungal resistance,"* Am. J. Med., 1996. **100**: p. 617.

73. Ofek, I and E H Beachey. *"Mannose binding and epithelial cell adherence of Escherichia coli,"* Infect. Immun., 1978. **22**(1): p. 247.

74. Ohshima, H and T Kondo. *"Approximate analytic expression for the electrophoretic mobility of colloidal particles with surface-charge layers,"* J. Coll. Int. Sci., 1989. **130**(1): p. 281.

75. Ong, Y-L, et al. *"Adhesion forces between E. coli bacteria and biomaterial surfaces,"* Langmuir, 1999. **15**: p. 2719.

76. Overbeek, J T G, in *Colloid Science*, H.R. Kruyt, Editor. 1952, Elsevier: Amsterdam. p. 266.

77. Palabiyikoglu, I, M Oral, and M Tulunay. *"Candida colonization in mechanically ventilated patients,"* J. Hosp. Infect., 2001. **47**: p. 239.

78. Pauling, L, *General Chemistry*. 3 ed. 1970, New York: Dover Publications.

79. Pedersen, K. *"Biofilm development on stainless steel and PVC surfaces in drinking water,"* Wat. Res., 1990. **24**(2): p. 239.

80. Razatos, A, et al. *"Force measurements between bacteria and poly(ethylene glycol)-coated surfaces,"* Langmuir, 2000. **16**: p. 9155.

81. Razatos, A, et al. *"Evaluating the interaction of bacteria with biomaterials using atomic force microscopy,"* J. Biomater. Sci. Polym. Ed., 1998. **9**(12): p. 1361.

82.   Reid, G. *"Microbial adhesion to biomaterials and infections of the urogenital tract,"* Coll. Surf. B: Biointerfaces, 1994. **2**: p. 377.

83.   Rijnaarts, H H M, et al. *"Reversibility and mechanism of bacterial adhesion,"* Coll. Surf. B: Biointerfaces, 1995. **4**: p. 5.

84.   Safdar, A, D S Perlin, and D Armstrong. *"Hematogenous infections due to Candida parapsilosis: changing trends in fungemic patients at a comprehensive cancer center during the last four decades,"* Diagn. Microbiol. Infect. Dis., 2002. **44**: p. 11.

85.   Schelenz, S and G French. *"An outbreak of multidrug-resistant Pseudomonas aeruginosa infection associated with contamination of bronchoscopes and and endoscope washer-disinfector,"* J. Hosp. Infect., 2000. **46**: p. 23.

86.   Schenkel, J H and J A Kitchener. *"A test of the Derjaguin-Verwey-Overbeek theory with a colloidal suspension,"* Trans. Faraday Soc., 1960. **56**: p. 161.

87.   Schierholz, J M and J Beuth. *"Implant infections: a haven for opportunistic bacteria,"* J. Hosp. Infect., 2001. **49**: p. 87.

88.   Sharon, N and H Lis. *"Lectins as cell recognition molecules,"* Science, 1989. **246**(4927): p. 227.

89.   Singh, R S, A K Tiwary, and J F Kennedy. *"Lectins: Sources, activities and applications,"* Crit. Rev. Biotechnol., 1999. **19**(2): p. 145.

90.   Sneddon, I N. *"The relation between load and penetration in the axisymmetric Boussinesq problem for a punch of arbitrary profile,"* Int. J. Eng. Sci., 1965. **3**: p. 47.

91.   Stover, K C, et al. *"Complete genome sequence of Pseudomonas aeruginosa PAO1: an opportunistic pathogen,"* Nature, 2000. **406**: p. 959.

92.   Suci, P A, J D Vrany, and M W Mittelman. *"Investigation of interactions between antimicrobial agents and bacterial biofilms using attenuated total reflection Fourier transform infrared spectroscopy,"* Biomater., 1998. **19**: p. 327.

93.   Surman, S B, et al. *"Comparison of microscope techniques for the examination of biofilms,"* J. Microbiol. Meth., 1996. **25**: p. 57.

94. Takashima, S and H Morisaki. *"Surface characteristics of the microbial cell of Pseudomonas syringae and its relevance to cell attachment,"* Coll. Surf. B: Biointerfaces, 1997. **9**: p. 205.

95. Touhami, A, et al. *"Probing specific lectin-carbohydrate interactions using atomic force microscopy imaging and force measurements,"* Langmuir, 2003. **19**(5): p. 1745.

96. Touhami, A, B Nysten, and Y F Dufrêne. *"Nanoscale mapping of elasticity of microbial cells by atomic force microscopy,"* Langmuir, 2003. **19**: p. 4539.

97. Vadillo-Rodriguez, V, et al. *"On relations between microscopic and macroscopic physicochemical properties of bacterial cell surfaces: An AFM study on Streptococcus mitis strains,"* Langmuir, 2003. **19**: p. 2372.

98. van der Aa, B C and Y F Dufrêne. *"In situ characterization of bacterial extracellular polymeric substance by AFM,"* Coll. Surf. B: Biointerfaces, 2002. **23**: p. 173.

99. van der Aa, B C, et al. *"Stretching cell surface macromolecules by atomic force microscopy,"* Langmuir, 2001. **17**: p. 3116.

100. van Oss, C J. *"Acid-base interfacial interactions in aqueous media,"* Coll. Surf. A, 1993. **78**: p. 1.

101. van Oss, C J, *Interfacial Forces in Aqueous Media*. 1994, New York, NY: Marcel Dekker, Inc.

102. van Oss, C J, M K Chaudhury, and R J Good. *"Additive and non-additive surface tension components and the interpretation of contact angles,"* Langmuir, 1988. **4**: p. 884.

103. Velegol, S B and B E Logan. *"Contributions of bacterial surface polymers, electrostatics and cell elasticity to the shape of AFM force curves,"* Langmuir, 2002. **18**: p. 5256.

104. Velegol, S B, et al. *"AFM imaging artifacts due to bacterial cell height and AFM tip geometry,"* Langmuir, 2003. **16**: p. 851.

105. Verwey, E J and J T G Overbeek, *Theory of the Stability of Lyophobic Colloids*. 1948, Amsterdam: Elsevier.

106. Vieira, M J, et al. *"Effect of metallic ions on the adhesion of biofilms formed by Pseudomonas fluorescens,"* Coll. Surf. B: Biointerfaces, 1993. **1**: p. 119.

107.   Vincent, J-L, et al. *"Epidemiology, diagnosis and treatment of systemic Candida infection in surgical patients under intensive care,"* Intensive Care Med., 1998. **24**: p. 206.

108.   von Smoluchowski, M. *"Versuch einer matematischen theorie dar koagulationskinetik kollider losungen,"* Z. Phys. Chem., 1918. **92**: p. 129.

109.   Wenzler, L A, et al. *"Measurements of single-molecule bond-rupture forces between self-assembled monolayers of organosilanes with the atomic force microscope,"* Langmuir, 1997. **13**: p. 3761.

110.   Winans, S C. *"Command, control and communication in bacterial pathogenesis,"* Trends Microbiol., 1998. **6**(10): p. 382.

111.   Wolfgang, M C, et al. *"Conservation of genome content and virulence determinants among clinical and environmental isolates of Pseudomonas aeruginosa,"* Proc. Natl. Acad. Sci. USA, 2003. **100**(14): p. 8484.

112.   Wu, W. *"Application of the extended DLVO theory - the stability of alatrofloxacin mesylate solutions,"* Coll. Surf. B: Biointerfaces, 1999. **14**: p. 57.

113. Wu, W, R F Giese, and C J van Oss. *"Stability versus flocculation of particle suspensions in water - correlation with the extended DLVO approach for aqueous systems, compared with the classical DLVO theory,"* Coll. Surf. B: Biointerfaces, 1999. **14**: p. 47.

114. *Gram Stain.* http://www.uphs.upenn.edu/bugdrug/antibiotic_manual/Gram1.htm, (Accessed 1 December, 2003).

115. ZoBell, C E and D Q Anderson. *"Observations on the multiplication of bacteria in different volumes of stored sea water and the influence of oxygen tension and solid surfaces,"* Biol. Bull. Woods Hole, 1936. **71**: p. 324.